Available online at www.sciencedirect.com
SCIENCE DIRECT®
Journal of Computational Physics 204 (2005) 319–352
JOURNAL OF COMPUTATIONAL PHYSICS
www.elsevier.com/locate/jcp

Improvement of convective concentration fluxes in a one step reactive flow solver

G. Billet *

ONERA BP 72-29, av. de la Division Leclerc, 92322 Châtillon Cedex, France

Received 3 June 2004; received in revised form 1 October 2004; accepted 11 October 2004
Available online 11 November 2004

Abstract

The MUSCL approach appeared 25 years ago. This extension of Godunov's scheme increases its accuracy. In order to restrict the amplitude of the gradients, it has been associated with nonlinear limiters (TVD conditions). Since then, the MUSCL-TVD couple has been widely used and improved. Pursuing our work in [J. Comput. Phys. 170 (2001) 161], where adaptive limiters have been considered, and in [Comput. Fluids 32 (2003) 1473], where a simple model preserving pressure and velocity across contact discontinuities in reactive flows has been proposed, we develop an optimal limiter for species convection. All these improvements are introduced in a one step scheme to simulate unsteady reactive flows for a wide range of Mach number. For $M \ll 1$, the present algorithm has been applied to a 1D premixed and diffusion flames and the results are compared with a DNS reactive code. The algorithm has also been validated on a 2D supersonic reactive flow concerning fuel break up and compared with high-order methods (ACM and wavelet filter schemes, WENO, pseudospectral). A planar acoustic wave interacting with circular and spherical diffusion flames is also analyzed. From these various cases, we show that accurate results can be obtained by using a one step algorithm which is definitely less expensive compared to multistage high-order schemes.

Keywords: MUSCL approach; TVD schemes; Navier–Stokes equations; Reactive flows; Unsteady flows; Acoustic waves; Shock waves

1. Introduction

The simulation of unsteady flows where very stiff phenomena occur requires that the algorithms have definite virtues. Particularly, when several reactive species are present in the flow, the strong gradients appearing across the flame have to be captured properly. It is necessary to use a method that is able to

* Fax: +33 1467 34266.
E-mail address: billet@onera.fr.

0021-9991/$ - see front matter © 2004 Elsevier Inc. All rights reserved.
doi:10.1016/j.jcp.2004.10.016

follow the physical and chemical events with good accuracy and stability if the wavelike oscillatory behavior has to be taken into account. This accuracy is also linked with the mesh refinement and consequently with the number of grid points, therefore the approach has to be easily vectorizable, parallelizable and to have a number of elementary operations as small as possible in order to have reasonable computational costs. At the end, if shock waves exist in the flow or may be formed, it is judicious to apply a 'shock capturing scheme'.

In usual practices all these constraints are not always satisfied, and in general, schemes are:

- either low-order accurate (lower or equal to 2) in order to reduce computing costs and stabilize the numerical solution,
- or high-order accurate associated with a computing cost and a risk of numerical oscillations appearance.

We propose here a method which combines low cost, good accuracy and stability. A one step algorithm has the advantage in reducing the number of elementary operations and consequently to produce a reduction of the computational cost but does the numerical solution preserve sufficient accuracy? We are going to attempt to answer to this question.

The hyperbolic terms of the Navier–Stokes equations are generally the most difficult parts to solve because of the presence of nonlinear terms. For these convective terms, adaptive limiters introduced in a MUSCL procedure [1] have been proposed in [2,3]. Their compressive properties suitably balance the diffusive effects of the flux splitting, such as for example $AUSM^+$ splitting [4]. These adaptive limiters give results comparable to that of precise schemes (ENO-family, Hermitian or pseudospectral schemes).

Let us consider the Euler equations for a binary mixture

$$U_t + f_x = 0 \quad \text{with } U = [\rho_1, \rho_2, \rho u, \rho E]^{\mathrm{T}}$$

discretized with an explicit finite difference scheme on an uniform grid mesh $x_j = j\Delta x$, with a time step δt defined as

$$\delta t = C_{cfl} \frac{\Delta x}{\underset{j}{\mathrm{Max}}(|u| + a)}, \tag{1}$$

with $0 < C_{cfl} < 1$ and a is the celerity of sound.

If we study directly the above-mentioned set of limiters on these equations, their good behavior is not easy to explain because of the interconnection of several factors (equations system, nonlinear equations, flux splitting, limiter expressions depending on local variations). But if we keep only one limiter and if we assume that velocity, temperature and pressure are constant and that species have the same molecular weight

$$u = cst, \quad T = cst, \quad p = cst, \quad W_1 = W_2$$

it becomes possible to understand the behavior of the TVD-MUSCL schemes and the influence of the limiter on the accuracy of the numerical solution. After this study on the hyperbolic part, we define a second order accuracy criterion on δt associated with the solving of the diffusive terms of Navier–Stokes equations and at last, 1D, 2D and 3D simulations are presented and compared (in 1D and 2D) with other approaches.

2. The convection equation

We consider a numerical approximation of the weak solution of the hyperbolic initial value problem (where $\rho = \rho_1 = \rho_2$):

$$\begin{aligned}
&\rho_t + f_x = 0,\\
&f = \rho u,\\
&\rho(x,0) = \rho_0(x),\\
&u = cst > 0.
\end{aligned} \tag{2}$$

The equivalent equation may be put on a formal basis through the use of Taylor-series expansion. The Mth order equivalent equation is given by

$$\rho_t + f_x + \sum_{m=0}^{m=M-1} (\Delta x^m E_x^{(m)} + \delta t^m E_t^{(m)}) + \mathrm{O}(\Delta x^M, \delta t^M) = 0.$$

To have a Mth order truncation error, the difference representation of the spatial derivatives is chosen so that the M first terms $\Delta x^m E_x^{(m)}$ and $\delta t^m E_t^{(m)}$ of the expansion are cancelled:

$$\rho_t + f_x + \sum_{m=0}^{m=M-1} (\underbrace{\Delta x^m E_x^{(m)}}_{=0} + \underbrace{\delta t^m E_t^{(m)}}_{=0}) + \mathrm{O}(\Delta x^M, \delta t^M) = 0.$$

There is another way to obtain a Mth order truncation error. It is enough to cancel the sum of the M first terms of the expansion or at least it is enough that the sum of the M first terms is on the same order than the truncation error:

$$\rho_t + f_x + \underbrace{\sum_{m=0}^{m=M-1} (\Delta x^m E_x^{(m)} + \delta t^m E_t^{(m)}) + \mathrm{O}(\Delta x^M, \delta t^M)}_{=\mathrm{O}(\Delta x^M, \delta t^M)} = 0.$$

From (1), $\delta t = \beta \Delta x$ (with $\beta \ll 1$) and we may rewrite

$$\rho_t + f_x + \underbrace{\sum_{m=0}^{m=M-1} E_m}_{=\mathrm{O}(\Delta x^M)} + \mathrm{O}(\Delta x^M) = 0, \tag{3}$$

with $E_m = \Delta x^m (E_x^{(m)} + \beta^m E_t^{(m)})$.

Definition 1. If $\|\sum_{m=0}^{m=M-1} E_m\| \leqslant \|E_M\|$, (3) is a Mth order approximation of (2).

Let $\rho_j^n = \rho(x_j, t^n)$, $x_j = j\Delta x$, $t^n = n\delta t$ denote a numerical approximation in conservation form. The scheme that generalizes Godunov's scheme and its second-order extension to any finite order of accuracy can be written in standard conservation form

$$\frac{\delta \rho_j}{\delta t} + \frac{\Delta F^n}{\Delta x} = \frac{\rho_j^{n+1} - \rho_j^n}{\delta t} + \frac{F_{j+1/2}^n - F_{j-1/2}^n}{\Delta x} = 0. \tag{4}$$

In the MUSCL approach, the numerical fluxes at t^n and at $(j+\frac{1}{2})\Delta x$ and at $(j-\frac{1}{2})\Delta x$ are expressed as

$$\begin{aligned}
&F_{j+1/2}^n = u\rho_{j+1/2}^n,\\
&F_{j-1/2}^n = u\rho_{j-1/2}^n
\end{aligned}$$

with the presence of limiter φ

$$\begin{aligned}
&\rho_{j+1/2}^n = \rho_j^n + \frac{\varphi(r_j)}{2}(\rho_{j+1}^n - \rho_j^n),\\
&\rho_{j-1/2}^n = \rho_{j-1}^n + \frac{\varphi(r_{j-1})}{2}(\rho_j^n - \rho_{j-1}^n)
\end{aligned} \tag{5}$$

and the slope ratio

$$r_j = \frac{\rho^n_j - \rho^n_{j-1}}{\rho^n_{j+1} - \rho^n_j}. \tag{6}$$

A fourth-order Taylor expansion of $F^n_{j+1/2}$ at node x_j (where $\rho_x \neq 0$ and $r \approx 1$) can be written as

$$F^n_{j+1/2} = f + \frac{\Delta x}{2} f' \rho_x + \frac{\Delta x^2}{8}[2(1-2\varphi')f'\rho_{xx} + f''\rho_x\rho_x] + \frac{\Delta x^3}{8}\left[\frac{2}{3}f'\rho_{xxx} + (1-2\varphi')f''\rho_x\rho_{xx} + 2\varphi'' f' \frac{\rho^2_{xx}}{\rho_x} + \frac{f'''}{6}\rho_x\rho_x\rho_x\right] + \mathrm{O}(\Delta x^4) \tag{7}$$

with $\varphi' = \frac{\mathrm{d}\varphi}{\mathrm{d}r}(r=1)$, $\varphi'' = \frac{\mathrm{d}^2\varphi}{\mathrm{d}r^2}(r=1)$.

From Eq. (2), $f' = \frac{\mathrm{d}f}{\mathrm{d}\rho} = u$, $f'' = f''' = 0$ and

$$F^n_{j+1/2} = f + \frac{\Delta x}{2} u\rho_x + \frac{\Delta x^2}{4}(1-2\varphi')u\rho_{xx} + \frac{\Delta x^3}{4}u\left(\frac{1}{3}\rho_{xxx} + \varphi''\frac{\rho^2_{xx}}{\rho_x}\right) + \mathrm{O}(\Delta x^4). \tag{8}$$

This expression is still intricate, particularly because of the last term $\varphi''\frac{\rho^2_{xx}}{\rho_x}$, and in order to cancel it we consider limiter

$$\varphi(r_j, \omega, \kappa) = 0 \quad \text{for } r_j < 0, \tag{9}$$

$$\varphi(r_j, \omega, \kappa) = \frac{1}{2}[(1-\kappa)\min(r_j, \omega) + (1+\kappa)\min(1, \omega r_j)] \quad \text{for } r \geqslant 0, \tag{10}$$

where ω and κ are parameters that verify

$$1 \leqslant \omega \leqslant \frac{3-\kappa}{1-\kappa} \quad \text{if } r_j > \omega \ (r_j \text{ large}), \tag{11}$$

$$1 \leqslant \omega \leqslant \frac{3-\kappa}{1+\kappa} \quad \text{if } 0 \leqslant r_j < 1 \text{ and } \omega r_j < 1. \tag{12}$$

This expression is well known ([5] or [6] for instance). When $\kappa = 1/3$, φ is a third-order interpolation of $\rho^n_{j+1/2}$ when r_j is close to 1. With conditions (11) and (12), φ lies in the TVD region defined by Sweby [7]. φ is a piecewise function formed from four linear functions (Fig. 1). The first derivative $\varphi' = cst$ on each interval $I_1 =]-\infty, 0]$, $I_2 =]0, \frac{1}{\omega}]$, $I_3 =]\frac{1}{\omega}, \omega]$ and $I_4 =]\omega, \infty[$ and the second derivative $\varphi'' = 0\ \forall r_j$. Therefore, the numerical flux (8) has this simpler form

$$F^n_{j+1/2} = f + \frac{\Delta x}{2}u\rho_x + \frac{\Delta x^2}{4}(1-2\varphi')u\rho_{xx} + \frac{\Delta x^3}{12}u\rho_{xxx} + \mathrm{O}(\Delta x^4)$$

when $r_j \approx 1$, and it becomes relatively easy to study the equivalent equation.

But when the couple (r_{j-1}, r_j) varies between $]-\infty, +\infty] \times]-\infty, +\infty]$ the analysis is more complicated. Let

$$\rho^{n+1}_j = H(\rho^n_{j-k_L}, \ldots, \rho^n_{j+k_R})$$

with $k_L = 0, 1, 2$ and $k_R = 0, 1$. The function H may be expressed on a double entry table depending on the slope ratio r_{j-1} and r_j (Fig. 2(a)). For instance, element H_{43} corresponds to $r_j \geqslant \omega$ and $\frac{1}{\omega} \leqslant r_{j-1} < \omega$. For these values of r, we have

$$\rho^n_{j+1/2} = \frac{(3-\kappa) - \omega(1-\kappa)}{4}\rho^n_j + \frac{(1+\kappa) + \omega(1-\kappa)}{4}\rho^n_{j+1},$$

$$\rho^n_{j-1/2} = \frac{1+\kappa}{4}\rho^n_j + \frac{2-\kappa}{2}\rho^n_{j-1} - \frac{1-\kappa}{4}\rho^n_{j-2}$$

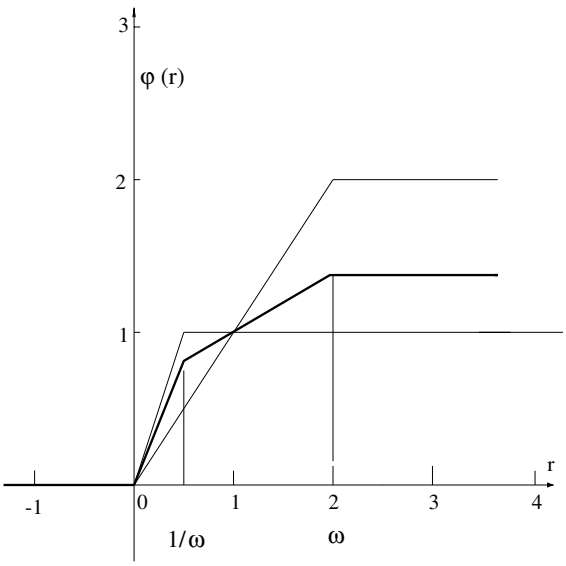

Fig. 1. Limiter φ with $\kappa = 1/3$.

and then, from (4)

$$\rho_j^{n+1} = -\frac{c}{4}(1-\kappa)\rho_{j-2}^n + \frac{c}{4}(4-2\kappa)\rho_{j-1}^n + \left\{1 - \frac{c}{4}[2-2\kappa-(1-\kappa)\omega]\right\}\rho_j^n - \frac{c}{4}[1+\kappa+(1-\kappa)\omega]\rho_{j+1}^n,$$

where $c = u\frac{\delta t}{\Delta x} = C_{cfl}\frac{u\Delta x}{\mathrm{Max}_j(|u|+a)}$, from (1). If the elements of H are written $H_{lk} = a_{-2}\rho_{j-2}^n + a_{-1}\rho_{j-1}^n + a_0\rho_j^n + a_1\rho_{j+1}^n$ the expressions of a_i for every H_{lk} can be summarized in the following table:

	a_{-2}	a_{-1}	a_0	a_1
H_{11}	0	c	$1-c$	0
H_{12}	$-\frac{c}{4}[1-\kappa+(1+\kappa)\omega]$	$\frac{c}{4}[5-\kappa+(1+\kappa)\omega]$	$1-c$	0
H_{13}	$-\frac{c}{4}(1-\kappa)$	$\frac{c}{2}(2-\kappa)$	$1-\frac{c}{4}(3-\kappa)$	0
H_{14}	0	$\frac{c}{4}[3-\kappa-(1-\kappa)\omega]$	$1-\frac{c}{4}[3-\kappa-(1-\kappa)\omega]$	0
H_{21}	0	$\frac{c}{4}[5-\kappa+(1+\kappa)\omega]$	$1-\frac{c}{4}[5-\kappa+(1+\kappa)\omega]$	0
H_{22}	$-\frac{c}{4}[1-\kappa+(1+\kappa)\omega]$	$\frac{c}{2}[3-\kappa+(1+\kappa)\omega]$	$1-\frac{c}{4}[5-\kappa+(1+\kappa)\omega]$	0
H_{23}	$-\frac{c}{4}[1-\kappa]$	$\frac{c}{4}[5-3\kappa+(1+\kappa)\omega]$	$1-\frac{c}{4}[4-2\kappa+(1+\kappa)\omega]$	0
H_{24}	0	$\frac{c}{4}[4-2\kappa+2\kappa\omega]$	$1-\frac{c}{4}[4-2\kappa+2\kappa\omega]$	0
H_{31}	0	$\frac{c}{4}[5-\kappa]$	$1-\frac{c}{4}[4-2\kappa]$	$-\frac{c}{4}[1+\kappa]$
H_{32}	$-\frac{c}{4}[1-\kappa+(1+\kappa)\omega]$	$\frac{c}{4}[6-2\kappa+(1+\kappa)\omega]$	$1-\frac{c}{4}[4-2\kappa]$	$-\frac{c}{4}[1+\kappa]$
H_{33}	$-\frac{c}{4}[1-\kappa]$	$\frac{c}{4}[5-3\kappa]$	$1-\frac{c}{4}[3-3\kappa]$	$-\frac{c}{4}[1+\kappa]$
H_{34}	0	$\frac{c}{4}[4-2\kappa-(1-\kappa)\omega]$	$1-\frac{c}{4}[3-3\kappa-(1-\kappa)\omega]$	$-\frac{c}{4}[1+\kappa]$
H_{41}	0	c	$1-\frac{c}{4}[3-\kappa-(1-\kappa)\omega]$	$-\frac{c}{4}[1+\kappa+(1-\kappa)\omega]$
H_{42}	$-\frac{c}{4}[1-\kappa+(1+\kappa)\omega]$	$\frac{c}{4}[5-\kappa+(1+\kappa)\omega]$	$1-\frac{c}{4}[3-\kappa-(1-\kappa)\omega]$	$-\frac{c}{4}[1+\kappa+(1-\kappa)\omega]$
H_{43}	$-\frac{c}{4}[1-\kappa]$	$\frac{c}{4}[4-2\kappa]$	$1-\frac{c}{4}[2-2\kappa-(1-\kappa)\omega]$	$-\frac{c}{4}[1+\kappa+(1-\kappa)\omega]$
H_{44}	0	$\frac{c}{4}[3-\kappa-(1-\kappa)\omega]$	$1-\frac{c}{4}[2-2\kappa-2(1-\kappa)\omega]$	$-\frac{c}{4}[1+\kappa+(1-\kappa)\omega]$

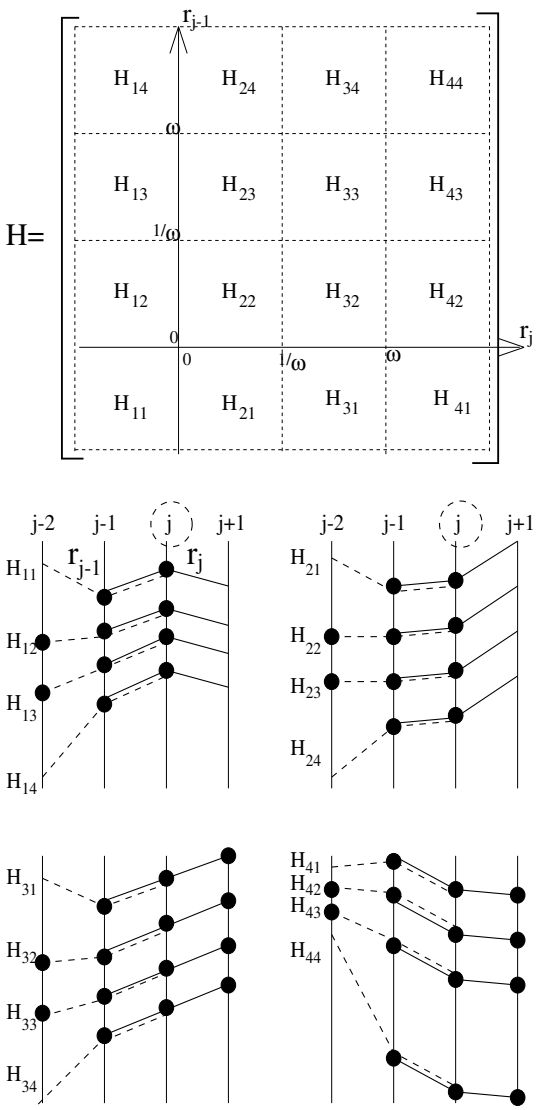

Fig. 2. Elements H_{lk} versus values of r_j and r_{j-1} and correspondence between elements H_{lk} and scheme stencil in function of the variation of ρ around x_j.

Depending on the couple (r_{j-1},r_j), we have a two-point, three-point or four-point scheme (Fig. 2(b)). The numerical flux is always consistent since $\forall l,k$

$$\sum_{i=-2}^{1} a_i = 1.$$

If the error term in time of the discretization of $\frac{\delta \rho_j}{\delta t}$ is introduced in the equivalent equation and if $\rho(x,t)$ is assumed to be a differentiable function of C^M, the equivalent equation at node x_j is written as

$$\frac{\rho_j^{n+1}-\rho_j^n}{\delta t}+\frac{F_{j+1/2}^n-F_{j-1/2}^n}{\Delta x}+=\rho_t+f_x+\underbrace{\left[-\frac{A_0}{4}u\rho_x\right]}_{E_0}+\underbrace{\left[-\frac{\Delta x}{8}u(A_1-4c)\rho_{xx}\right]}_{E_1}$$
$$+\underbrace{\left[-\frac{\Delta x^2}{24}u(A_2+4c^2)\rho_{xxx}\right]}_{E_2}+\underbrace{\sum_{m=3}^{m=M}\Delta x^m(\cdot)}_{\sum_{m=3}^{m=M}E_m}=0. \tag{13}$$

Tables $A_m = A_m(r_j, r_{j-1}, \omega, \kappa)$ with $m = 0,1,2$ are represented in Fig. 3 (where $\alpha = \omega - 1$).

3. General case ($\rho_x \neq 0$, $\rho_{xx} \neq 0$, $\rho_{xxx} \neq 0$)

We introduce the following properties.

3.1. First-order scheme

From Definition 1, we may write: the scheme is at least a first-order scheme if $\|E_0\| \leqslant \|E_1\|$. With the L^1-norm for example, this condition may be expressed as

$$\left|\frac{\Delta x}{2}(A_1-4c)\rho_{xx}\right| \geqslant |A_0\rho_x|.$$

If we replace the derivatives by their centered difference approximation we get

$$\left|\frac{\Delta x}{2}(A_1-4c)\left[\frac{\nabla_c\rho}{\Delta x^2}+\mathrm{O}(\Delta x^2)\right]\right| \geqslant \left|A_0\left[\frac{\Delta_c\rho}{2\Delta x}+\mathrm{O}(\Delta x^2)\right]\right|$$

with $\nabla_c\rho = \rho_{j+1}^n - 2\rho_j^n + \rho_{j-1}^n$ and $\Delta_c\rho = \rho_{j+1}^n - \rho_{j-1}^n$. If we only consider the O(1) terms we deduce:

Proposition 1. *Eq. (4) is at least a first-order approximation of (2) if* $T_1 = |(A_1 - 4c)\nabla_c\rho| - |A_0\Delta_c\rho| \geqslant 0$.

3.2. Second-order scheme

From Definition 1, we may write: the scheme is at least a second-order scheme if $\|E_0 + E_1\| \leqslant \|E_2\|$. If we introduce the centered difference approximation of ρ_{xxx}, with the L^1-norm we may write

$$\left|\frac{\Delta x^2}{24}(A_2+4c^2)\left(\frac{\square_c\rho}{2\Delta x^3}+\mathrm{O}(\Delta x^2)\right)\right| - \left|\frac{\Delta x}{8}(A_1-4c)\left(\frac{\nabla_c\rho}{\Delta x^2}+\mathrm{O}(\Delta x^2)\right)+\frac{A_0}{4}\left(\frac{\Delta_c\rho}{2\Delta x}+\mathrm{O}(\Delta x^2)\right)\right| \geqslant 0$$

with $\square_c\rho = \rho_{j+2}^n - 2\rho_{j+1}^n + 2\rho_{j-1}^n - \rho_{j-2}^n$. If we only consider the O(1) terms, we deduce:

Proposition 2. *Eq. (4) is at least a second-order approximation of (2) if*

$$T_2 = \underbrace{\left|\frac{A_2+4c^2}{6}\square_c\rho\right|}_{T_2^{(2)}(\omega,\kappa)} - \underbrace{|(A_1-4c)\nabla_c\rho + A_0\Delta_c\rho|}_{T_2^{(1)}(\omega,\kappa)} \geqslant 0. \tag{14}$$

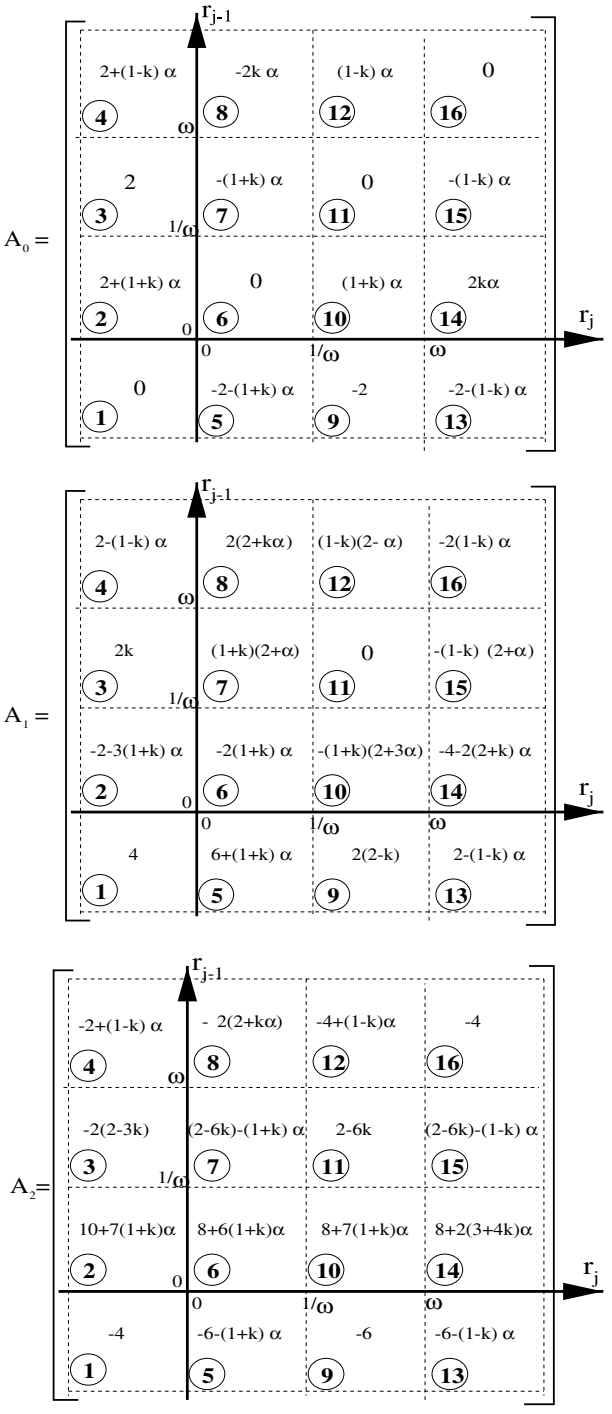

Fig. 3. Tables A_0, A_1 and A_2.

3.3. Third-order scheme

The scheme is at least a third-order scheme if $\|E_0 + E_1 + E_2\| \leqslant \|E_3\|$.

As a second-order time scheme is sufficient, we only take into account the space accuracy. If $\kappa = 1/3$, the scheme is a third-order scheme in space when $(r_{j-1}, r_j) \in I_3 \times I_3$. This result is well known ([5] for instance) and we adopt this value in the rest of this paper.

3.4. Minimization of lower-order error terms

During an interval of time $[t_1,t_2]$, T_2 may be negative for some values of t and the scheme is then at most a first-order one. To minimize the lower error term, when $T_2 < 0$, we introduce the following proposition:

Proposition 3. *Let* $0 \leqslant n < Int[\frac{(t_2-t_1)}{\delta t}]$, $m \geqslant 1$ (n *and* $m \in \mathbb{N}^*$) *and* $t_1 + (n+m)\delta t \leqslant t_2$, *we define* $\Omega = \bigcup_n [t_1 + n\delta t, t_1 + (n+m)\delta t]$ *such that for any* $t \in \Omega$, $T_2(t) < 0$ (*at most a first-order scheme*). *Then there exists a value of* ω *such that* $T(\omega) = \int_\Omega |T_2^{(1)}(\omega, \kappa = 1/3)|\, \mathrm{d}t$ *is minimal.*

This optimal value will be determined by a parametric study in a following section.

4. Particular cases

Several scenarii have to be considered. If at node x_j

(1) $\rho_x = 0$, $\rho_{xx} \neq 0$ and $\rho_{xxx} = 0$, the scheme is at least a first-order scheme,
(2) $\rho_x = 0$, $\rho_{xx} \neq 0$ and $\rho_{xxx} \neq 0$, the scheme is at least a first-order scheme,
(3) $\rho_x \neq 0$, $\rho_{xx} \neq 0$ and $\rho_{xxx} = 0$, the scheme is at least a first-order scheme if $A_0 \equiv 0$,
(4) $\rho_x = 0$, $\rho_{xx} = 0$ and $\rho_{xxx} \neq 0$, the scheme is at least a second-order scheme,
(5) $\rho_x \neq 0$, $\rho_{xx} = 0$ and $\rho_{xxx} \neq 0$, the scheme is at least a second-order scheme if $A_0 \equiv 0$,
(6) $\rho_x = 0$, $\rho_{xx} = 0$ and $\rho_{xxx} = 0$, the scheme is at least a third-order scheme,
(7) $\rho_x \neq 0$, $\rho_{xx} = 0$ and $\rho_{xxx} = 0$, the scheme is at least a third-order scheme if $A_0 \equiv 0$,

$A_0 \equiv 0$ at node x_j

- for a monotone function ($r_{j-1} \geqslant 0$ and $r_j \geqslant 0$) if r_{j-1} and r_j lie in the same interval $I_n (n = 1,\ldots,4)$ (elements 6, 11 and 16 of Fig. 3),
- for two consecutive extremum, $r_{j-1} < 0$ and $r_j < 0$ (element 1).

$A_0 \neq 0$, therefore the scheme sets up a zero order dispersive error at node x_j,

- for a monotone function ($r_{j-1} \geqslant 0$ and $r_j \geqslant 0$) if r_{j-1} and r_j lie in different intervals I_n,
- for an isolated extremum at node x_{j-1} ($r_{j-1} < 0$ and $r_j > 0$) since, in this case, $\rho_x \neq 0$ and $A_0 \neq 0$.

5. Parametric analysis of the scheme

5.1. Convection of waves

We study the convection of a sharp gaussian profile and a smooth profile (dome shape) initially 20 cells wide (Figs. 6 and 7). The grid mesh is constant and the Courant number $C_{cfl} = 0.5$. The Mach number is

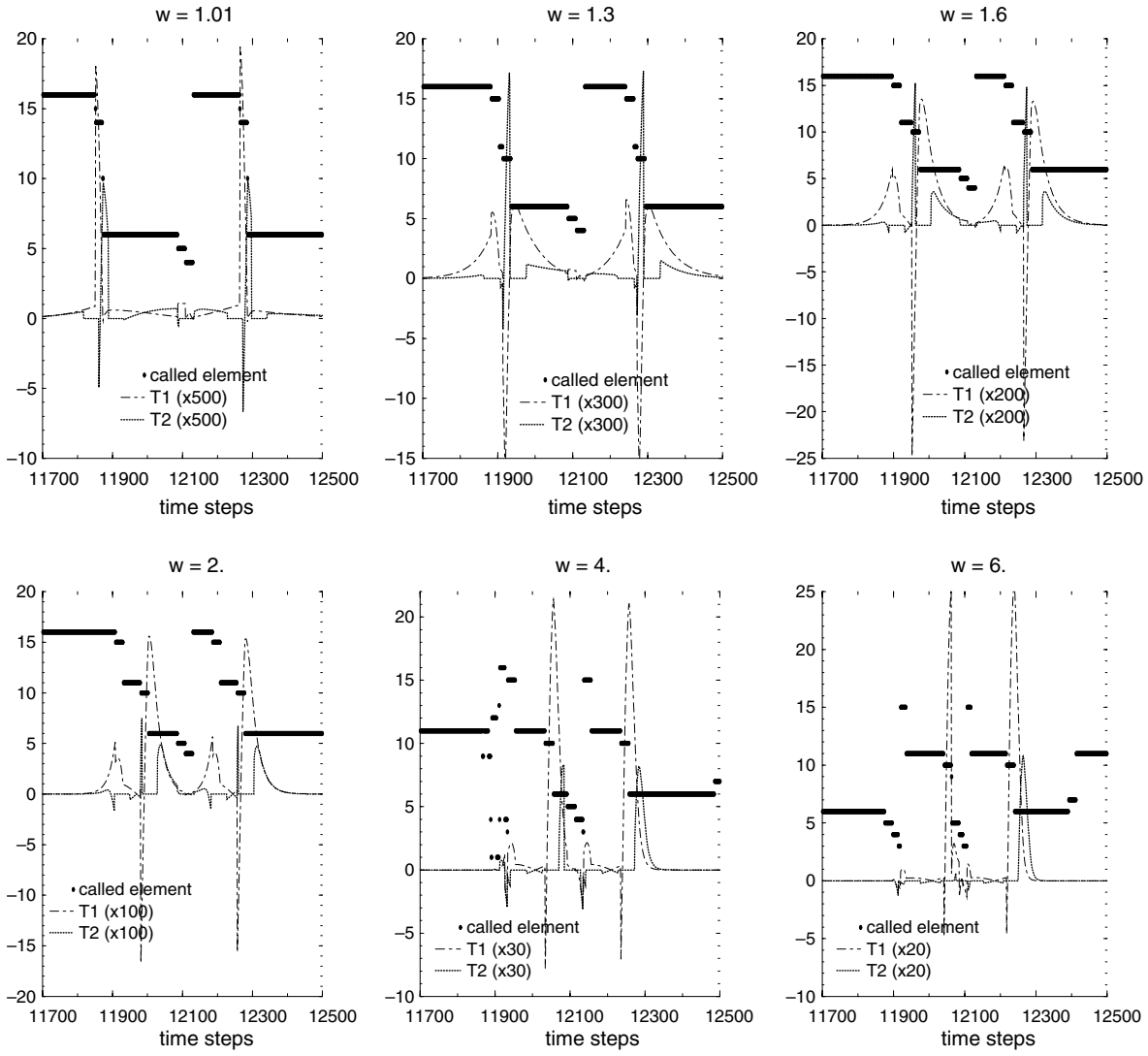

Fig. 4. Sharp profile. Called elements of A_m and errors T_1 and T_2.

$M = 0.1$. Six different values of ω are chosen with two further away from unity ($\omega = 1.01$, 1.3, 1.6, 2, 4 and 6). With the last two values, φ is not completely included in the *TVD*-Sweby domain if conditions (11) and (12) are not applied. The development of the numerical solution in function of time at a given control point $x_c = 60$ mm is analyzed. The study starts at $t_1 = 11700\delta t$ when scalar ρ begins to growth at x_c and ends at $t_2 = 12{,}500\delta t$ when ρ falls down to zero at the same point x_c.

Fig. 4 presents the elements of A_m activated by the algorithm during the time integration. When a circle is filled in with value 16 for example, this means that element 16 of A_m (Fig. 3) is activated. The evolution of terms T_1 and T_2 during $[t_1,t_2]$ at x_c for the six values of ω and for the sharp profile (the variations of T_1 and T_2 are similar for the dome shape) are presented in the same figure. For $\omega \leqslant 2$, the order of activated elements are about the same but with $\omega = 4$ and $\omega = 6$ elements becomes much more complex (particularly for $\omega = 4$). In Fig. 4, the values of T_1 and T_2 are not multiplied by the

same constant for each ω and we remark that T_1, T_2 and also Ω (defined in Proposition 3) grow when ω increases. For $\omega \leqslant 1.6$, $T_2 \geqslant 0$ when $T_1 < 0$ and therefore, even when $T_1 < 0$ the scheme is at least a second order scheme. For $\omega \geqslant 2$, $T_2 = 0$ when $T_1 < 0$ and, in this case, the scheme becomes more and more compressive and may even set up a dispersive error when the variations of T_1 and T_2 are not the same along the first branch of the profile ($11{,}700\delta t \leqslant t \leqslant 12{,}100\delta t$) and the second branch ($12{,}100\delta t \leqslant t \leqslant 12{,}500\delta t$). This behavior appears for $\omega = 4$ and is accentuated for $\omega = 6$. We have drawn $T(\omega)$ in Fig. 5. The region where the dissipative error is high is indicated ($1 \leqslant \omega \leqslant 1.2$). The zones where the scheme becomes compressive ($2.5 \leqslant \omega \leqslant 4$) and where the dispersive error predominates ($\omega > 4$) are presented. The values of ω which minimize T is $\omega = 1.45$ for the sharp profile and $\omega = 1.4$ for the smooth profile.

The numerical solutions are plotted for different values of ω at $t_3 = 18{,}000\delta t$ (Figs. 6 and 7) for both profiles. The profiles are sharper when ω increases (from 1 to 4). With $\omega = 6$, the solution sets up instabilities due to the predominance of dispersive error. Both extremum go on growing with the time (see the arrows in Fig. 6).

From this study, we deduce if the variations of u and p are weak, the optimal value of (ω,κ) are (1.45, 1/3).

6. Extension to two species convection

Two species with different molecular weights are convected. The physical problem remains simple if we study only the convection of these species but the mathematical resolution is more complicated than in the previous example. We study the influence of the interpolated variables on the numerical solution.

6.1. Equation system

Velocity u ($u > 0$), pressure p, temperature T and the ratio of constant-pressure specific heat γ are assumed constant. The Euler equations are reduced to

$$(\rho_1)_t + u(\rho_1)_x = 0, \tag{15}$$

$$(\rho_2)_t + u(\rho_2)_x = 0. \tag{16}$$

6.2. Space discretization

The discrete form of Eqs. (15) and (16) depends on the choice of the interpolated variables at interface $j + \frac{1}{2}$. We have chosen two variable sets quite similar:

- the first one is named $\mathrm{MUSCL}_{\{\rho_i\}} = \{u, p, T, \rho_1\}^{\mathrm{T}}$,
- the second one is called $\mathrm{MUSCL}_{\{Y_i\}} = \{u, p, T, Y_1\}^{\mathrm{T}}$, with $Y_1 = \frac{\rho_1}{\rho_1+\rho_2}$.

6.2.1. $MUSCL_{\{\rho_i\}}$

This set uses one of the mass concentrations. With the MUSCL approach, we have $u_{j+1/2} = u$, $p_{j+1/2} = p$, $T_{j+1/2} = T$ which are constant and only $\rho_{1_{j+1/2}}$ varies. Therefore,

$$\rho_{2_{j+1/2}} = \frac{W_2}{\Re}\left(\frac{p}{T} - \frac{\Re\rho_{1_{j+1/2}}}{W_1}\right),$$

with $\Re$ the universal gas constant.

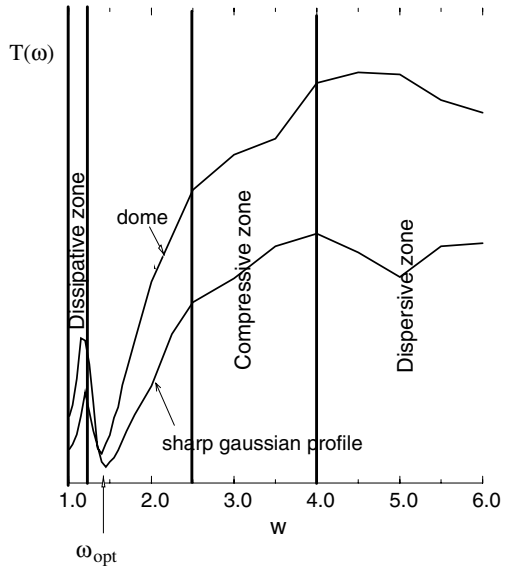

Fig. 5. Variation of $T(\omega)$ for a convection equation.

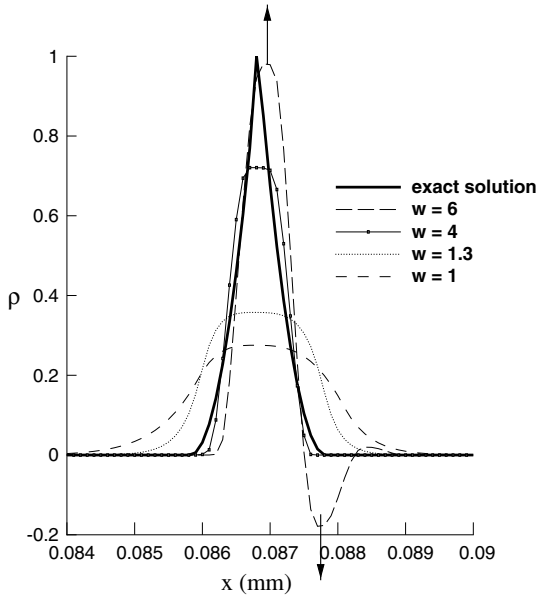

Fig. 6. Sharp profile. Exact and numerical solutions at $t_3 = 18{,}000\delta t$.

6.2.2. MUSCL$_{\{Y_i\}}$

This set uses one of the mass fractions. With the above, we again have $u_{j+1/2} = u$, $p_{j+1/2} = p$, $T_{j+1/2} = T$ which are constant and only $Y_{1_{j+1/2}}$ varies. We deduce

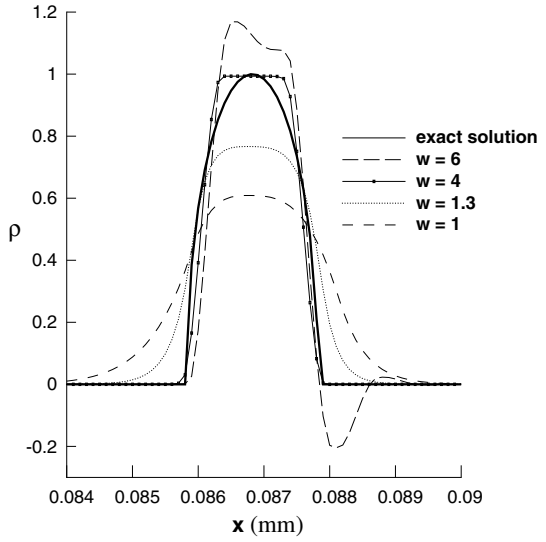

Fig. 7. Smooth profile. Exact and numerical solutions at $t_3 = 18{,}000\delta t$.

$$
\begin{aligned}
Y_{2_{j+1/2}} &= 1 - Y_{1_{j+1/2}}, \\
\rho_{1_{j+1/2}} &= \frac{C_2 Y_{1_{j+1/2}}}{C_{21} Y_{1_{j+1/2}} + 1}, \\
\rho_{2_{j+1/2}} &= \frac{C_1 Y_{2_{j+1/2}}}{C_{12} Y_{2_{j+1/2}} + 1},
\end{aligned}
\tag{17}
$$

where $C_1 = \frac{pW_1}{\Re T}$, $C_{21} = \frac{W_2}{W_1} - 1$, $C_2 = \frac{pW_2}{\Re T}$, $C_{12} = \frac{W_1}{W_2} - 1$ are constant.

6.3. Equivalent system

6.3.1. MUSCL$_{\{\rho_i\}}$

With this set, the equivalent system is similar to Eq. (13) whatever the ratio of the molecular weights:

$$(\rho_i)_t + u(\rho_i)_x = \frac{A_0}{4} u(\rho_i)_x + \frac{\Delta x}{8} u(A_1 - 4c)(\rho_i)_{xx} + \frac{\Delta x^2}{24} u(A_2 + 4c^2)(\rho_i)_{xxx} + \mathrm{O}(\Delta x^3) \quad \text{for } i = 1, 2.$$

The behavior of the solution will be identical to that of Eq. (13).

6.3.2. MUSCL$_{\{Y_i\}}$

With this interpolation set, the expression of the equivalent system becomes more complex because Y_1 is present in the numerator and the denominator of the expression (17). If we express the first and second derivatives of ρ_1,

$$
\begin{aligned}
(\rho_1)_x &= \frac{C_2}{(C_{21} Y_1 + 1)^2} (Y_1)_x, \\
(\rho_1)_{xx} &= \frac{C_2}{(C_{21} Y_1 + 1)^2} \left[(Y_1)_{xx} - \frac{2C_{21}}{C_{21} Y_1 + 1} (Y_1)_x (Y_1)_x \right],
\end{aligned}
$$

an additional term in $(\rho_1)_{xx}$ appears that is still present in the equivalent system:

$$(\rho_i)_t + u(\rho_i)_x = \frac{A_0}{4}u(\rho_i)_x + \frac{\Delta x}{8}u\left\{\widetilde{A}_i(\rho_i)_x(\rho_i)_x + [A_1(C_{ji}Y_i+1)^2 - 4c](\rho_i)_{xx}\right\} + \mathrm{O}(\Delta x^2) \tag{18}$$

with $i = 1,2$, $\widetilde{A}_i = \widetilde{A}_i(\omega, C_i, C_{ji}, Y_i)$ where $j \neq i$.

The expressions of the elements of $\widetilde{A}_i$ are relatively complicated. When the molecular weights are close, terms $\widetilde{A}_i$ and C_{ji} cancel and the equivalent system (18) is similar to Eq. (13). Therefore, the behavior of the solution is the same as in the previous section. But, when the W_i are very different, these terms are not negligible anymore.

6.4. Results

We apply the analytical results to a convection at $M = 0.1$ of a sharp profile of the hydrogen mass fraction Y_1 ($W_1 = 2.016$) in a surrounding oxygen flow ($W_2 = 32$). With this shape of Y_1, the profile of $\rho_1 = \rho Y_1$ seems like a dome. The spot is initially 20 cells wide and is convected with $C_{cfl} = 0.5$. We have chosen $\omega = 4$. In Fig. 8, the exact solution and the numerical solutions of Y_1 and ρ_1, with both sets of interpolated variables, are examined after $50{,}000\delta t$. With $\mathrm{MUSCL}_{\{Y_i\}}$, Y_1 and ρ_1 have lost their symmetric shape while with $\mathrm{MUSCL}_{\{\rho_i\}}$, the profiles keep their symmetric shapes and the maximum value is better conserved. This difference seems to come from the different expressions of the equivalent system because terms $\widetilde{A}_i$, which appear in (18), may have large values which greatly modify the error terms.

7. Time step criterion for a convection–diffusion equation

We have seen that a one step scheme has sufficient accuracy for a convection equation thanks to the properties of the limiter in the expression of convective fluxes but this limiter is not present in the viscous fluxes. In this case, what are the conditions so that a one step scheme applied to a convection–diffusion equation still remains a second-order accurate scheme?

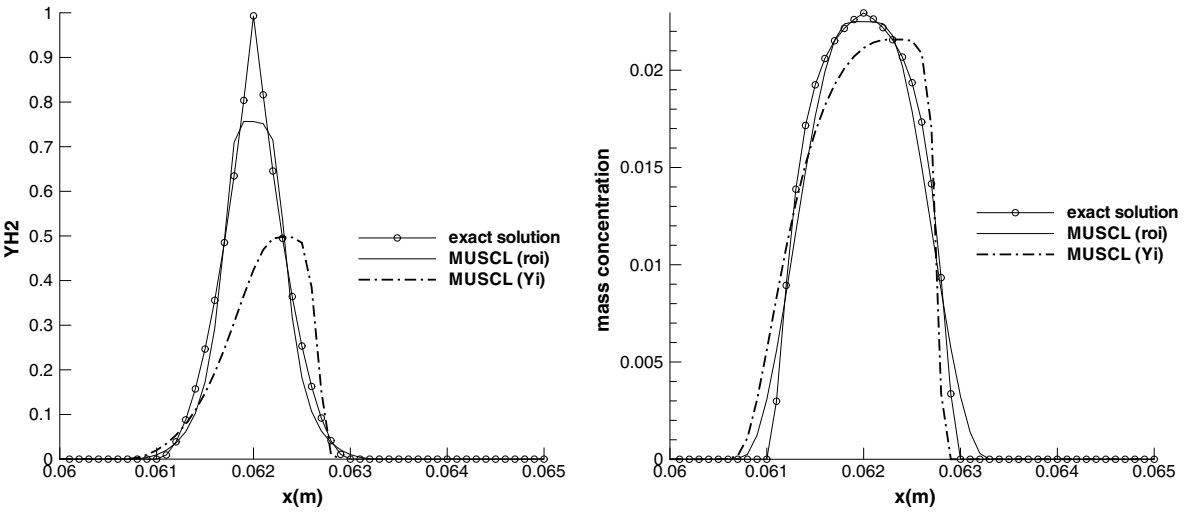

Fig. 8. Exact and numerical solutions $t = 50{,}000\delta t$.

Take again Eq. (2) where we introduce a diffusion term

$$\rho_t + u\rho_x = \varepsilon\rho_{xx} \tag{19}$$

with $\varepsilon = cst > 0$. Let a time splitting method

$$\rho_j^{n+2} = (\pounds_P(\delta t)\pounds_H(\delta t))\rho_j^n, \tag{20}$$

where $\pounds_H$ and $\pounds_P$ are the operators that solve the hyperbolic and parabolic parts of (19), respectively. Using a forward-difference representation for the time derivative and a central-difference representation for the second derivative, the equivalent equation for $\pounds_P$ is

$$\frac{\rho_j^{n+2}-\rho_j^{n+1}}{\delta t} - \varepsilon\frac{\rho_{j+1}^{n+1}-2\rho_j^{n+1}+\rho_{j-1}^{n+1}}{\Delta x^2} = \rho_t - \varepsilon\rho_{xx} + \left(\frac{\varepsilon^2}{2}\delta t - \frac{\varepsilon}{12}\Delta x^2\right)\rho_{xxxx} + \frac{\varepsilon^3}{6}\delta t^2\rho_{xxxxxx} + \cdots. \tag{21}$$

The well-known condition of linear stability is $\delta t \leqslant \frac{\Delta x^2}{2\varepsilon}$. If we assume $\varepsilon \ll 1$, we may neglect the last term of the RHS of (21). To have a second-order approximation of (19) we introduce a more restrictive condition:

Proposition 4. *If $\varepsilon \ll 1$, (21) is a second-order approximation of the parabolic part of (19) if the magnitude of the first-order error is weaker than the magnitude of the second-order error*:

$$\left\|\frac{\varepsilon^2}{2}\delta t\rho_{xxxx}\right\| \leqslant \left\|\frac{\varepsilon}{12}\Delta x^2\rho_{xxxx}\right\|.$$

With the L^1-norm, for instance, this condition may be written $\delta t \leqslant \frac{\Delta x^2}{6\varepsilon}$. This condition is three times more restrictive than the stability criterion.

Globally, to have a second-order approximation of (20), δt has to fulfill

$$\delta t \leqslant \ \mathrm{Min}\left(C_{cfl}\frac{\Delta x}{\mathrm{Max}_j(|u|+a)}, \frac{\Delta x^2}{6\varepsilon}\right).$$

An empirical study shows that the scheme (20) is stable for $C_{cfl} \leqslant 0.7$.

8. Conservation equations for multicomponent reacting flows

Navier–Stokes equations are written, where subscript α (resp. β and γ) represents the three space directions x, y and z:

$$\begin{aligned}
&(V)_t + (f)_\alpha = S \text{ with}\\
&V = \begin{bmatrix}\rho Y_i\\ \rho u_\beta\\ \rho_E\end{bmatrix}, \quad f = \begin{bmatrix}\rho Y_i u_\alpha + J_\alpha^i\\ \rho u_\alpha u_\beta + p\delta_{\alpha\beta} - \tau_{\alpha\beta}\\ Eu_\alpha + p\delta_{\alpha\beta}u_\beta - u_\beta\tau_{\alpha\beta} + J_\alpha^h\end{bmatrix}, \quad S = \begin{bmatrix}\overset{\circ}{\omega}_i\\ 0\\ 0\end{bmatrix},\\
&\tau_{\alpha\beta} = \left(\frac{2}{3}\bar{\mu} - \bar{\kappa}\right)\delta_{\alpha\beta}(u_\gamma)_\gamma - \bar{\mu}\Big((u_\alpha)_\beta + (u_\beta)_\alpha\Big),\\
&J_\alpha^i = \rho Y_i V_\alpha^{\mathrm{d}i}, \quad J_\alpha^h = -\bar{\lambda}T_\alpha + \sum_{i=1}^N h_i J_\alpha^i + \Re T\sum_{i=1}^N\sum_{j=1}^N \frac{X_j D_i^{\mathrm{T}}}{W_i D_{ij}}(V_\alpha^{\mathrm{d}i} - V_\alpha^{\mathrm{d}j}),\\
&V(\alpha,0) = V^0(\alpha), \quad -\infty < \alpha < +\infty, \ t \geqslant 0,
\end{aligned} \tag{22}$$

where ρ, Y_i, u_α, p, T, E and H represent the density, the mass fraction of species $i (i = 1,\ldots,N)$, the α-component of the velocity, the static pressure, the temperature, the total energy and the total enthalpy. In this paper, the third term (Dufour effects) of the RHS of J_α^h and the bulk viscosity of the mixture $\bar{\kappa}$ are neglected.

To close this system, the equation of state, the total energy, the specific heat at constant pressure, the conservation of the mass are given by:

$$p = \rho \Re T \sum_{i=1}^{N} \frac{Y_i}{W_i},$$

$$E = \sum_{i=1}^{N} \left(h_{i_0} Y_i + \int_{T_0}^{T} Y_i C_{\mathrm{P}_i}(s)\, \mathrm{d}s \right) - \frac{p}{\rho} + \frac{u_\alpha^2}{2},$$

$$C_{\mathrm{P}} = \sum_{i=1}^{N} Y_i C_{\mathrm{P}_i}, \quad \sum_{i=1}^{N} Y_i = 1,$$

where h_{i_0} and T_0 are the heat and temperature formations for species i, C_{P_i} the specific heat at constant pressure of species i and $\Re$ the universal gas constant. ω_i° represent the production rates. The viscosity $\bar{\mu}$ and the thermal conductivity $\bar{\lambda}$ of the mixture are expressed as

$$\bar{\mu} = \frac{1}{2} \left[\sum_{i=1}^{N} X_i \mu_i + \left(\sum_{i=1}^{N} \frac{X_i}{\mu_i} \right)^{-1} \right],$$

$$\bar{\lambda} = \frac{1}{2} \left[\sum_{i=1}^{N} X_i \lambda_i + \left(\sum_{i=1}^{N} \frac{X_i}{\lambda_i} \right)^{-1} \right],$$

where μ_i and λ_i are the viscosity and the thermal conductivity of the pure species i and

$$X_i = \frac{\frac{Y_i}{W_i}}{\sum_{j=1}^{N} \frac{Y_j}{W_j}}.$$

The μ_i and λ_i are obtained by a fourth-order polynomial in T.

Each C_{P_i} is determined by a continuous piecewise linear function in temperature based on JANAF tables:

$$C_{\mathrm{P}_i} = a_i^k T + b_i^k$$

with a_i^k and b_i^k constants on the interval of temperature $I_k = [(k-1)T^\Delta, kT^\Delta]$, $k = 1, 2, 3, \ldots$ and $T^\Delta = 10$ K. When $T \in I_m$, enthalpy h_i is expressed as

$$h_i = h_{i_0} + \sum_{k=1}^{m} \int_{T_{k-1}}^{T_k} (a_i^k s + b_i^k)\, \mathrm{d}s + \int_{T_m}^{T} (a_i^m s + b_i^m)\, \mathrm{d}s = h_{i_0}^{m'} + \int_{T_m}^{T} (a_i^m s + b_i^m)\, \mathrm{d}s.$$

In the last interval I_m, the linear evolution of C_{P_i} is replaced by a constant evolution $C_{\mathrm{P}_i} = \overline{b_i^m}$ because of the double flux approach [3]. So as to keep the correct value of h_i, the expression of $\overline{b_i^m}$ is given by

$$\overline{b_i^m} = \frac{a_i^m}{2}(T + T_m) + b_i^m.$$

Writing $h_{i_0}^m = h_{i_0}^{m'} - \overline{b_i^m} T_m$ and $h_0^m = \sum_{i=1}^{N} h_{i_0}^m Y_i$, E is expressed as

$$\begin{aligned} E &= h_0^m + \sum_{i=1}^{N} \overline{b_i^m} Y_i T - \frac{p}{\rho} + \frac{u_\alpha^2}{2} \\ &= h_0^m + C_{\mathrm{p}} T - \frac{p}{\rho} + \frac{u_\alpha^2}{2} \\ &= h_0^m + \frac{p}{\rho(\gamma - 1)} + \frac{u_\alpha^2}{2}. \end{aligned}$$

Diffusion velocity V_α^{di} of species i is represented by the expression

$$V_\alpha^{di} = -\frac{D_i}{Y_i}\left[(X_i)_\alpha + \Theta_i\frac{(T)_\alpha}{T} + (Y_i - X_i)\frac{(p)_\alpha}{p}\right], \quad D_i = \frac{1-Y_i}{\sum_{j\neq i}\frac{X_j}{D_{ij}}}\left(\frac{Y_i}{X_i}\right). \tag{23}$$

A correction velocity

$$V_\alpha^{cor} = \sum_{j=1}^{j=N} D_j\left[(X_j)_\alpha + \Theta_j\frac{(T)_\alpha}{T} - (Y_j - X_j)\frac{(p)_\alpha}{p}\right]$$

is added to the convecting field u_α to ensure the compatibility of species and mass conservation equations. Diffusion coefficient D_i of species i into the mixture is obtained from the binary mass diffusion coefficients D_{ij} calculated from [8]

$$D_{ij} = \frac{A_{ij}}{\mathscr{N}}T^{B_{ij}},$$
$$\mathscr{N} = \sum_{i=1}^{i=N}\frac{\rho Y_i}{W_i}.$$

The thermal diffusion is activated when there are large differences between the atomic masses of the constituent species (by instance for the hydrogen–oxygen combustion). Thermal diffusion rate Θ_i of species i into the mixture is estimated from

$$\Theta_i = \frac{\sum_{j\neq i}Y_j}{\sum_{j\neq i}X_j}\sum_{j\neq i}\theta_{ij} \quad \text{with } \theta_{ij} = d_{ij}^{T}\frac{W_j - W_i}{W_j + W_i}X_iX_j.$$

Coefficients d_{ij}^{T} are obtained from a tabulation [9].

A time-splitting method is used. The 3D finite difference operator is split into a product of simpler explicit operators:

$$V_j^{n+2} = \left(\pounds_H\left(\frac{\delta t}{3}\right)\pounds_P\left(\frac{\delta t}{3}\right)\pounds_S\left(\frac{\delta t}{3}\right)\pounds_P\left(\frac{\delta t}{3}\right)\pounds_H\left(\frac{\delta t}{3}\right)\right)V_j^n, \tag{24}$$

where $\pounds_H$, $\pounds_P$ and $\pounds_S$ are the operators associated with the hyperbolic, parabolic and source terms of the Navier–Stokes (NS) equations. This splitting allows the different parts of the NS equations to be solved with specific algorithms or specific hypotheses. The "double flux model" presented in [3] preserving pressure and velocity across the contact discontinuities is used in $\pounds_H$. All the diffusion and dissipation terms (operator $\pounds_P$) are solved with a centered second-order scheme similar to scheme (21). The simulations have been performed with a one step scheme (Euler's scheme) for all the operators.

8.1. Chemical kinetics

A chemical reaction mechanism for H_2–O_2 flames involving nine species (H_2, O_2, H_2O, H_2O_2, HO_2, OH, H, O, N_2) and 19 elementary reactions is considered [10] (CHEMKIN interpreter input):

R_1	$H_2 + O_2 \rightleftarrows 2OH$	1.7×10^{13}	0.	47,780
R_2	$H_2 + OH \rightleftarrows H_2O + H$	1.17×10^{9}	1.3	3626
R_3	$H + O_2 \rightleftarrows OH + O$	5.13×10^{16}	−0.816	16,507
R_4	$O + H_2 \rightleftarrows OH + H$	1.8×10^{10}	1.0	8826
R_5	$H + O_2 + M \rightleftarrows HO_2 + M$	2.1×10^{18}	−1.0	0
	H_2/3.3/O_2/0./N_2/0./H_2O/21./			

R_6	$H + 2O_2 \rightleftarrows HO_2 + O_2$	6.7×10^{19}	-1.42	0
R_7	$H + O_2 + N_2 \rightleftarrows HO_2 + N_2$	6.7×10^{19}	-1.42	0
R_8	$OH + HO_2 \rightleftarrows H_2O + O_2$	5.0×10^{13}	0	1000
R_9	$H + HO_2 \rightleftarrows 2OH$	2.5×10^{14}	0	1900
R_{10}	$O + HO_2 \rightleftarrows O_2 + OH$	4.8×10^{13}	0	1000
R_{11}	$2OH \rightleftarrows O + H_2O$	6.0×10^{8}	1.3	0
R_{12}	$H_2 + M \rightleftarrows H + H + M$ H_2/3./H/2./H_2O/6./	2.23×10^{12}	0.5	92,600
R_{13}	$O_2 + M \rightleftarrows O + O + M$	1.85×10^{11}	0.5	95,560
R_{14}	$H + OH + M \rightleftarrows H_2O + M$ H_2O/20./	7.5×10^{23}	-2.6	0
R_{15}	$HO_2 + H \rightleftarrows H_2 + O_2$	2.5×10^{13}	0.	700
R_{16}	$2HO_2 \rightleftarrows H_2O_2 + O_2$	2.0×10^{12}	0.	0
R_{17}	$H_2O_2 + M \rightleftarrows OH+OH+M$	1.3×10^{17}	0.	45,500
R_{18}	$H_2O_2 + H \rightleftarrows H_2 + HO_2$	1.6×10^{12}	0.	3800
R_{19}	$H_2O_2 + OH \rightleftarrows H_2O + HO_2$	1.0×10^{13}	0.	1800

8.2. Time step criterion

The time step has to verify the following stability condition:

$$\delta t = \mathrm{Min}\{\delta t_a, \delta t_d, \delta t_c\}$$

with (Courant criterion)

$$\delta t_a \leqslant C_{cfl} \min_{\alpha,j} \left(\frac{\Delta\alpha}{|u_\alpha| + a} \right). \tag{25}$$

If C_p and C_v are assumed constant, the Fourier criterion may be expressed as [11,12]

$$\delta t_d \leqslant \mathrm{Min}\left[\min_{\alpha,j} \left(\frac{\rho C_v}{2\bar{\lambda}} \Delta\alpha^2 \right), \min_{\alpha,j} \left(\frac{14\rho\Delta\alpha^2}{\bar{\mu}[8 + \Delta\alpha^2(\frac{1}{\Delta\beta^2} + \frac{1}{\Delta\gamma^2})]} \right) \right], \quad \gamma \neq \beta \neq \alpha.$$

δt_c is the time associated with the chemical process. When the chemical reactions are activated, the variation of some species during a time step are limited by empirical criteria. As in [9], we have chosen the following conditions on species HO_2 and H_2O_2:

$$|\delta Y_{HO_2}| \leqslant 10^{-6}, \tag{26}$$

$$|\delta Y_{H_2O_2}| \leqslant 10^{-7}. \tag{27}$$

These constraints have to be verified at every grid point during δt_c, otherwise δt_c is divided by two and so on, in order to have a reasonable variation of these species during δt_c.

If we assume that Proposition 4 is still valid for the NS equations we may write

Proposition 5. *Eq. (24) is a second-order approximation of (22) for* $\mathfrak{L}_H$ *and* $\mathfrak{L}_P$ *if*

$$\delta t = \mathrm{Min}\left\{ \delta t_a, \frac{\delta t_d}{3}, \delta t_c \right\} \quad \text{and} \quad \frac{\bar{\lambda}}{\rho C_p} \ll 1. \tag{28}$$

9. Numerical examples

We have studied 1D flows (convection of non-reactive and reactive fronts), 2D flows (acoustic wave – circular diffusion flame interaction, shock – hydrogen bubble interaction) and 3D flow (acoustic wave – spherical diffusion flame interaction). 1D results have been compared with solutions obtained from a DNS code [9] on the same grids and with identical time steps and initial conditions. This DNS code is a finite difference code solving the fully compressible Navier–Stokes equations for reacting flows with detailed chemistry and transport properties. Derivatives are computed using sixth-order centered explicit schemes. The temporal integration is realized with a fourth-order Runge–Kutta algorithm. This code will be noted RK4 in this paper and our approach RK1 because of the one step algorithm. In RK1, we adapt the limiter to the flow field. We use the limiter defined in (9) and (10) for all the variables when the pressure fluctuations are weak ($\Delta p/p < 0.002$) with $\kappa = 1/3$ and $\omega = 1.45$. When $\Delta p/p \geqslant 0.002$, the φ_{triad} [2,3] is activated except for the shocks where the first-order AUSM$^+$ scheme ($\varphi = 0$) is applied to avoid the overshoot and the spurious oscillations behind the shock. For all the simulations, condition (28) is fulfilled. All the gradients of (23) are taken into account except for the 1D diffusion flame simulation.

Results concerning the interaction between a shock and a circular hydrogen bubble and obtained with RK1 are compared with results coming from an ENO finite difference scheme and a Chebyshev collocation method [13] and also from a WENO and ACM-wavelet filter scheme [14].

9.1. 1D convection of an inert front H_2–O_2

For this first case, the Euler equations are solved. The front H_2–O_2 is convected with a constant velocity $u = 20$ m/s in a uniform pressure field $p = 1$ atm. At $t = 0$, the front thickness is 0.7 mm. $T_{H_2} = 1000$ K and $T_{O_2} = 2000$ K. The run parameters are set as: CFL = 0.5, $\Delta x = 100$ μm and $\delta t \approx 210^{-8}$ s. We compare the numerical and exact solutions of the hydrogen mass fraction at $t = 410^{-4}$ s (Fig. 9(a)). The front is convected with the correct velocity and remains smooth. The numerical diffusion is weak. To have a better quantitative information about the numerical diffusion, we compare our simulation with the solution

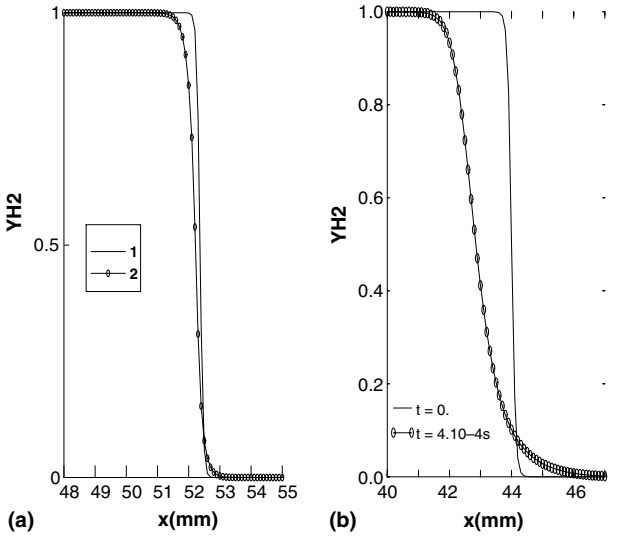

Fig. 9. 1D convection of an inert front; hydrogen mass fraction: (a) (1) – exact solution and (2) – numerical solution at $t = 4 \times 10^{-4}$ s; (b) DNS solution at $t = 0$ and $t = 4 \times 10^{-4}$ s.

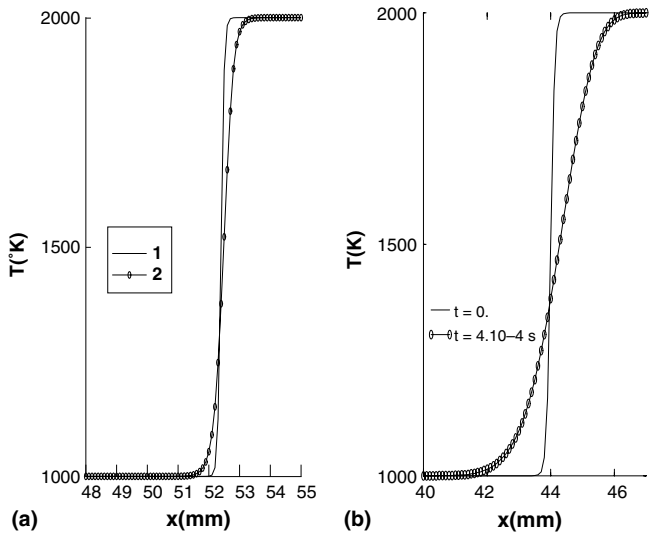

Fig. 10. 1D convection of an inert front; temperature: (a) (1) – exact solution and (2) – numerical solution at $t = 4 \times 10^{-4}$ s; (b) DNS solution at $t = 0$ and $t = 4 \times 10^{-4}$ s.

obtained from RK4. With this computation, numerical diffusion of the mass fractions and temperature (Figs. 9(a) and 10(a)) of our approach can be compared at the same time with the molecular mass and thermal diffusions of the front (Figs. 9(b) and 10(b)). The physical diffusions have spread the front on about 6 mm for the species and the temperature while the numerical diffusion has spread them on 1.5 mm. The numerical diffusion of the proposed algorithm is clearly less than the physical diffusions. This conclusion is also verified when the molecular weights are close to each other (O_2 and N_2 for example) and for very different velocities (this case has been performed with $0.5 \leqslant u \leqslant 1800$ m/s).

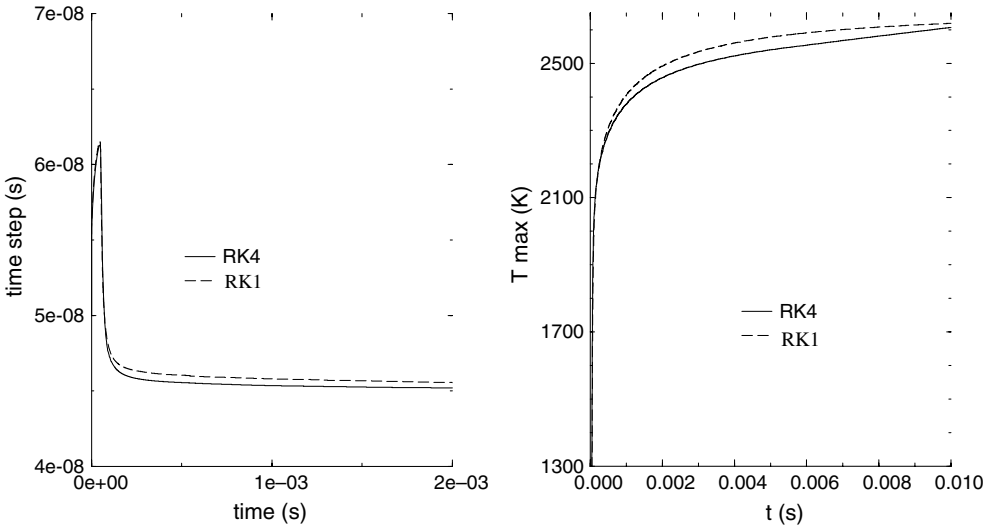

Fig. 11. (Left) time step variation at the beginning of the simulation; (right) T_{max} variation during the simulation.

9.2. 1D diffusion flame

In this simulation, we assume $Le_i = 1$ and the barodiffusion and the Soret effects are not activated. The length of the domain is $L = 4$ cm and mesh size $\Delta x = 100$ μm. Time step $\delta t = 4.510^{-8}$ s. We compare our approach with RK4. At $t = 0$, the simulations start with a diffusion zone spread over six cells around $x = 2$ cm. We take $Y_{H_2} = 0.233$ on the fuel side at $T = 300$K and $Y_{O_2} = 0.233$ at $T = 1300$ K on the oxidizer side. The static pressure is uniform ($p = 1$ atm) and velocity $u = 7$ cm/s. The treatment at the boundaries relies on

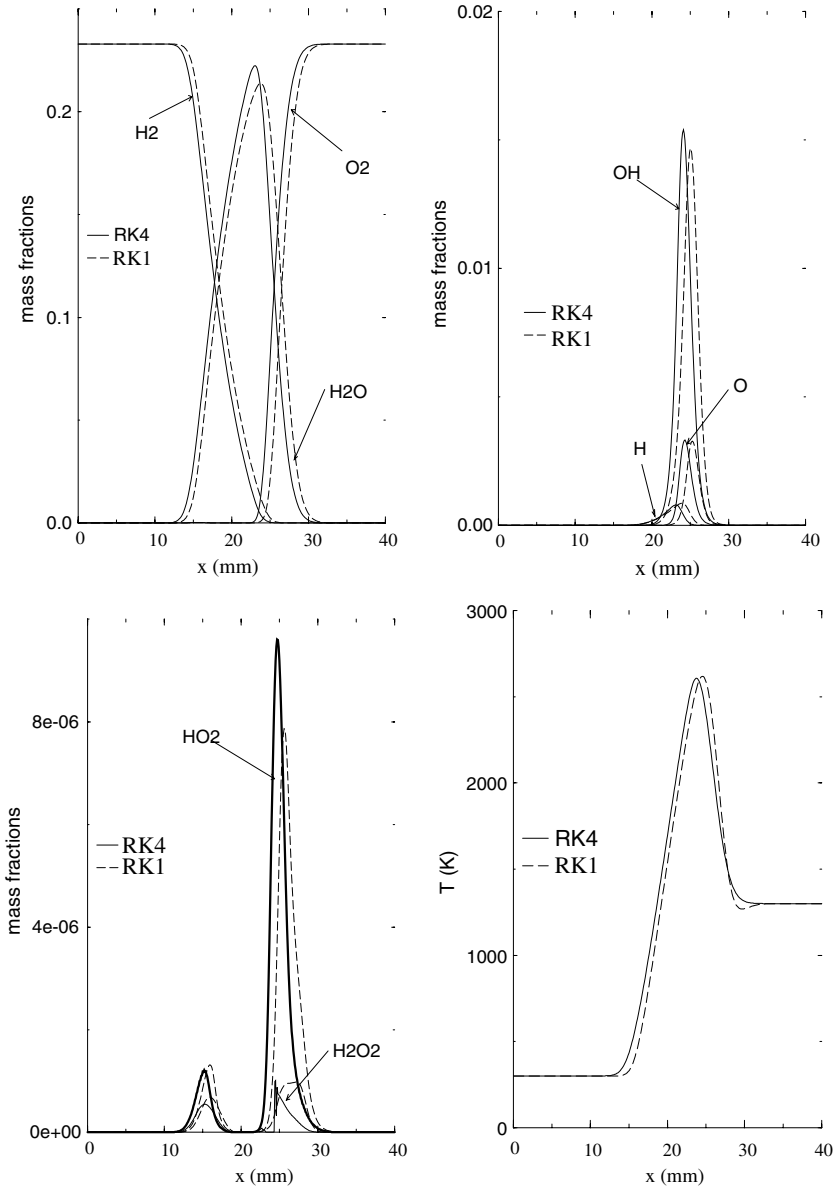

Fig. 12. Mass fraction profiles and temperature at $t = 10^{-2}$ s for the diffusion flame.

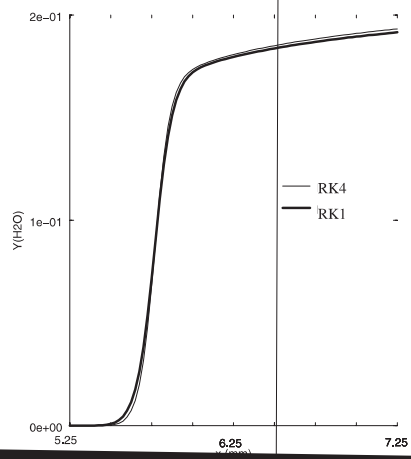
2e−01
1e−01
0e+00
Y(H2O)
RK4
RK1
5.25
6.25
7.25

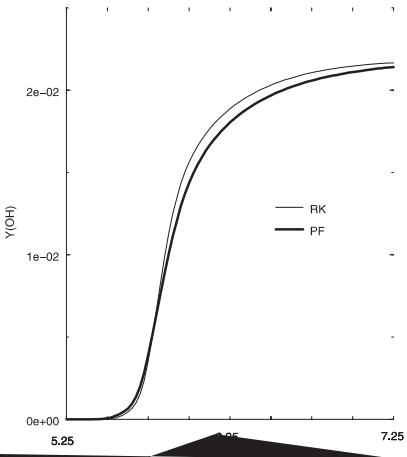
2e−02
1e−02
0e+00
Y(OH)
RK
PF
5.25
7.25

NSCBC technique [15]. Both boundaries are assumed to be non-reflective outlet planes. Time step and maximum temperature versus time, obtained with both codes, are plotted in Fig. 11. The greatest difference on T_{max} is equal to 40 K at $t \approx 4 \times 10^{-3}$ s.

The temperature and the species at $t = 10^{-2}$ s are drawn in Fig. 12 and the relative difference of the species productions $\int_0^L Y_i \, dx$, at this same time, between RK1 and RK4 are reported below:

	H_2O	OH	O	H	HO_2	H_2O_2
$\left\|\frac{RK1-RK4}{RK4}\right\|(\%)$	1	7	12	8	11	60

The shift of the profiles in Fig. 12 comes from a slight difference between the velocity fields during the computations. The relative errors are acceptable. Only, the production of the radical H_2O_2 presents a significant difference, mainly due to the beginning of an oscillating behavior of the RK4 solution near the value $x = 24$ mm.

9.3. 1D premixed flame

We investigate a $H_2/O_2/N_2$ premixed flame. Fresh gases are in the left side of the domain ($Y_{H_2} = 0.02621$, $Y_{O_2} = 0.297$, $Y_{N_2} = 0.67679$). At the left boundary, $T = 800$ K and $u = 14.57$ m/s. The initial pressure in the field is $p = 1$ atm. The domain length and mesh size are $L = 2$ cm and $\Delta x = 25$ μm. Time step is fixed to 6×10^{-9} s. The burnt gases and the temperature near the flame front are plotted in Figs. 13 and 14 and compared with the results obtained with RK4, at $t = 6 \times 10^{-4}$ s (=100,000δt). The curves are very close with a spreading slightly more accentuated in the approach presented here (approximately 30 μm $\approx \Delta x$). The difference of temperature in the burnt gases is 40 K between both simulations. Our results agree reasonably well with that of RK4. With these last two computations where operator $\pounds_P$ acts, the numerical diffusion of the algorithms is clearly weaker than the physical diffusion.

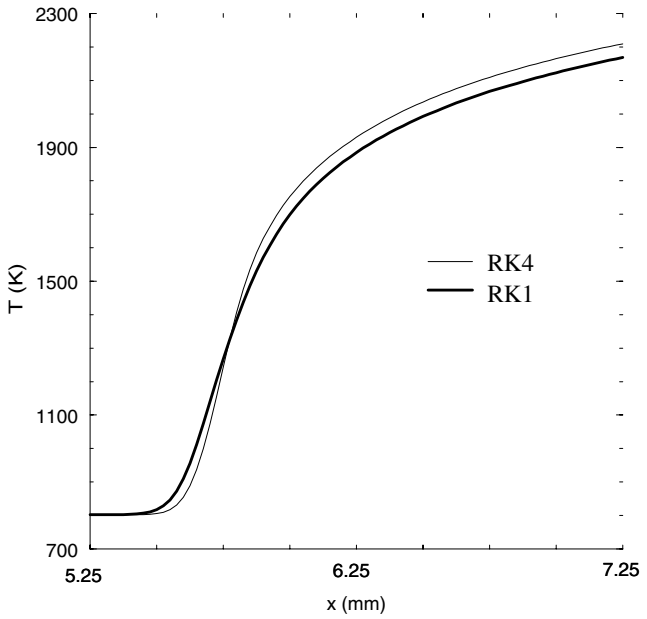

Fig. 14. Temperature profile for the premixed flame.

9.4. Planar acoustic wave interacting with a circular diffusion flame

The size of the square domain is $L = 4$ cm with 401 equidistant points in each direction for the grid mesh. We compute the interaction of a circular diffusion flame with pure hydrogen at $T = 300$ K inside a bubble surrounded by air at $T = 1500$ K at $t = 0$. The bubble is centered at ($x = 21$ mm, $y = 20$ mm) and its radius (where the temperature of the flame is maximum) is 5 mm. The pressure is uniform and equal to 1 atm and the velocity is null. A gaussian acoustic wave (positive pulse) moves in the domain across the x-direction. The wavelength of this perturbation is short and equivalent to the thickness of the flame ($\approx$2 mm) at the time where the interaction occurs. The maximum acoustic pressure and acoustic velocity are equal to 1750 Pa and 9 m/s. This would model situations observed for high-frequency combustion instabilities. Time step $\delta t = 6 \times 10^{-9}$ s is driven by the chemical process. As in [16], we carry out two identical simulations, one with and one without introducing the acoustic wave. The results are recorded at the same time and by a simple difference between both results, we plot the influence of the acoustic wave/diffusion flame interaction. The acoustic pressure distribution after the interaction is presented in Fig. 15. The result shows the different waves that issue from the interaction (incident wave, diffracted wave, reflected waves) and the caustics at $t = 3.94 \times 10^{-4}$ s. The two reflected waves, in spite of their weak amplitudes are well represented.

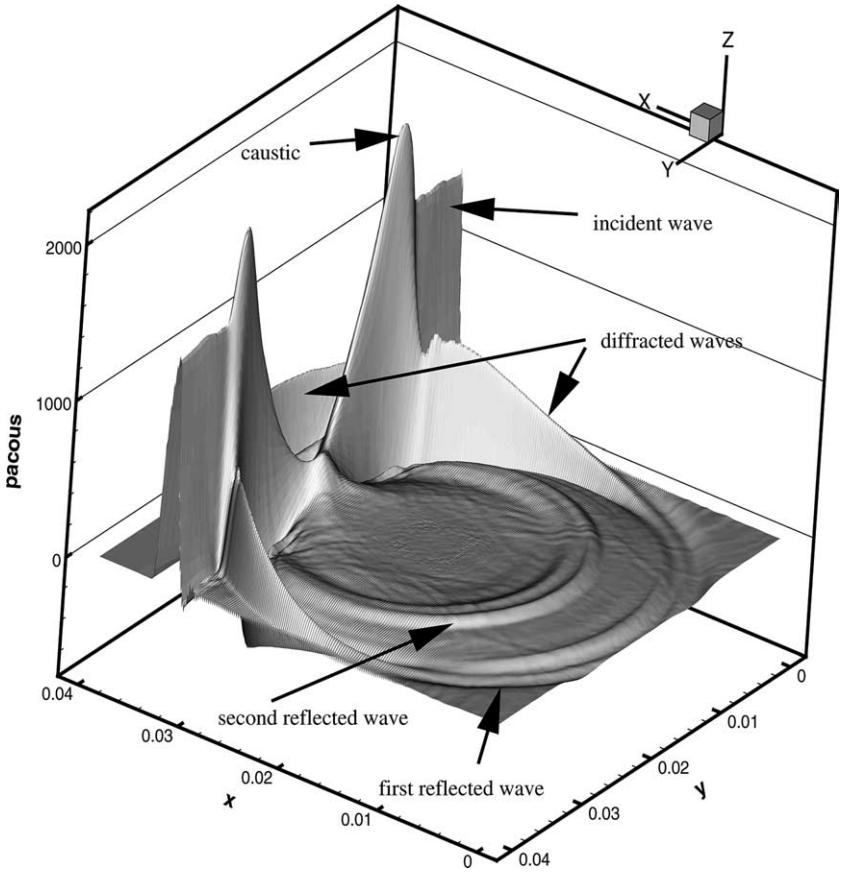

Fig. 15. Acoustic pressure at the end of the interaction between the circular diffusion flame and the thin acoustic wave.

The simulation has been performed again with a thicker gaussian acoustic wave (≈10 mm) which has the same amplitude. The result is displayed in Fig. 16. The characteristics of the flow after the interaction are not so visible because the wave is thicker than the flame. We have displayed, at the same time, the acoustic pressure in different sections $y = cst$ and compared the amplitude of the waves with the initial amplitude ($t = 0$) for both cases (Fig. 17). We have an amplification near caustics ($y = 9.3$ mm for the shorter wave length and $y = 7.3$ mm for the second wave) and a damping in the region $y = 0$.

9.5. Planar acoustic wave interacting with a spherical diffusion flame

The previous simulation is extended to 3D. The size of the parallelepiped domain is 1.8 cm × 1 cm × 1 cm in x-, y- and z-directions with $\Delta x = \Delta y = \Delta z = 100$ μm. A gaussian acoustic wave is intersecting a spherical flame located at the center of the domain. In y- and z-directions, periodic conditions are applied on the boundaries and NSCBC technique is used in x-direction. We present this interaction when the wave has nearly crossed the flame at a time where the thicknesses of the flame and wave are, respectively, 2 and 5 mm. Only the lower values of the acoustic pressure ($-100 \leqslant p_{\text{acous}} \leqslant 100$ Pa) are drawn in Fig. 18 in order to have a good visualization of the reflected waves. The code reproduces well the spherical wave expansion. The dome shape of the diffracted wave is well reproduced too.

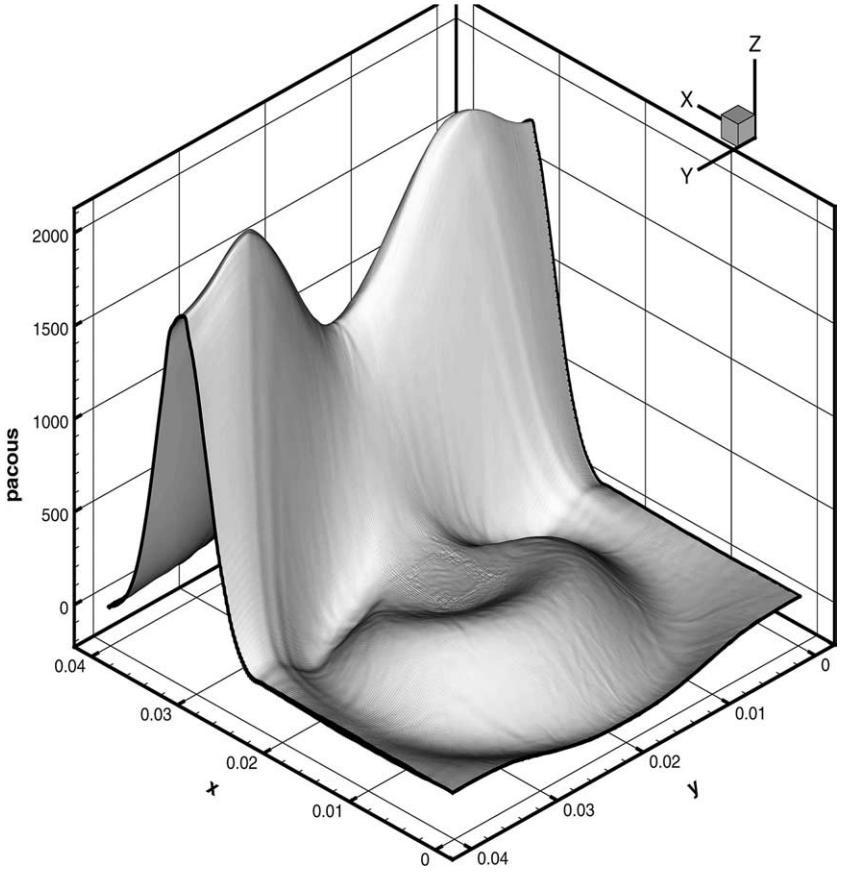

Fig. 16. Acoustic pressure at the end of the interaction between the circular diffusion flame and the thick acoustic wave.

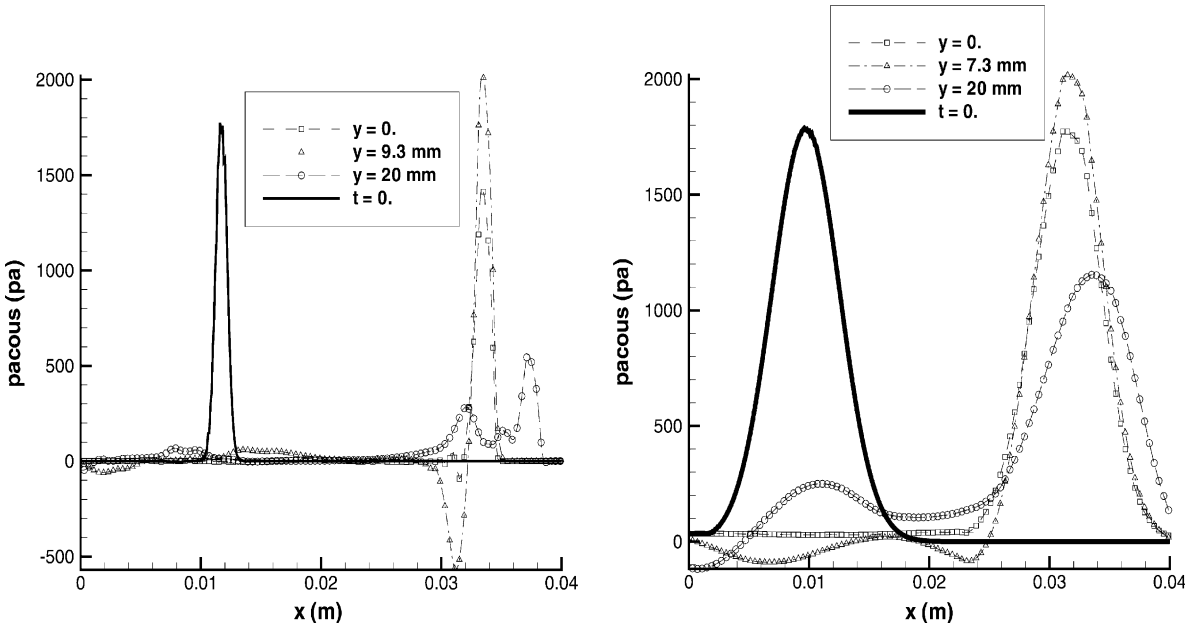

Fig. 17. Acoustic pressure at different sections at $t = 3.94 \times 10^{-4}$ s; interaction of the flame with thin and thick waves.

The time variation of heat release $Hr = \int_v (\sum h_i \dot{\omega}_i)$ (where V is the volume of the computational domain) is plotted for two different time intervals in Fig. 19. The first one [$t_1 = 6.1 \times 10^{-5}$ s, $t_2 = 7.6 \times 10^{-5}$ s] corresponds with the moment where the variation of T_{max} is very stiff and, at this

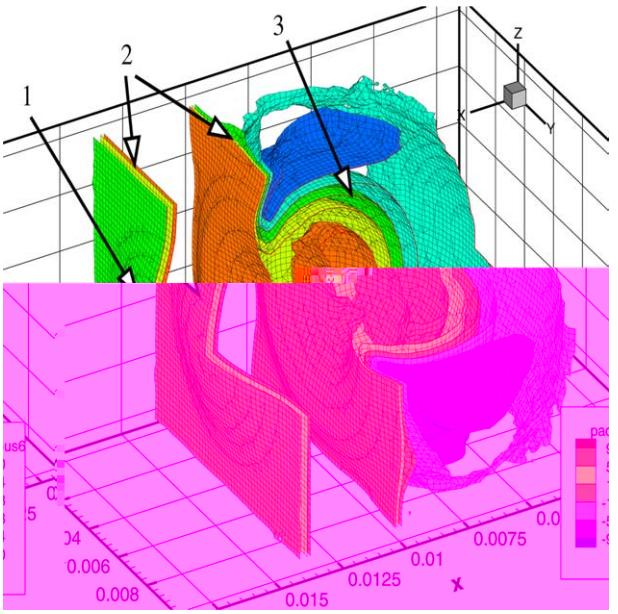

Fig. 18. Acoustic pressure at the end of the interaction between a spherical diffusion flame and the acoustic wave: (1) diffracted wave, (2) extremities of the incident wave, (3) reflected waves.

time, the flame thickness is about 2 mm and the mean radius of the flame is 3 mm (Fig. 19(a)). During the second period of time [$t_3 = 3.7 \times 10^{-4}$ s, $t_4 = 3.9 \times 10^{-4}$ s], T_{max} reaches 2430 K and the radius of the flame is about 5.2 mm. When wave and flame thicknesses are about the same, we only have an

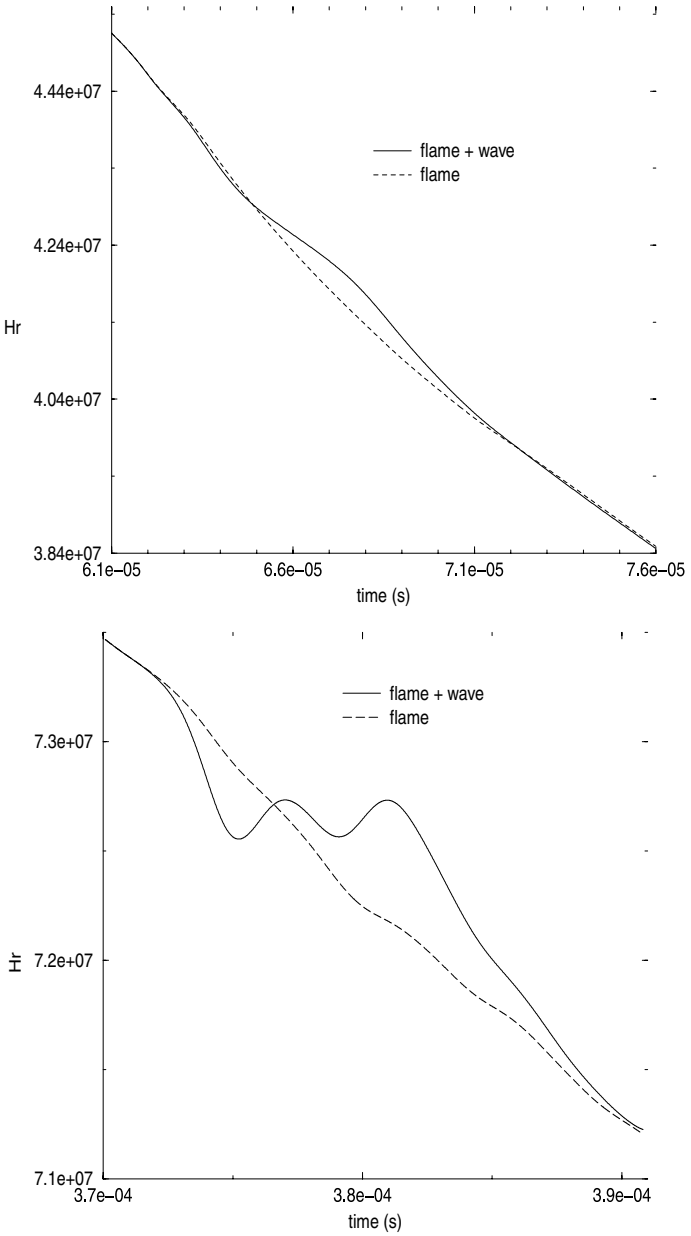

Fig. 19. Time variation of heat release rate: (left) at the start of the reactions; (right) when the chemical process is completely developed.

increase of *Hr* but, in the second case where the flame is thicker, the variation of *Hr* presents, at first, a drop of the heat release followed by a growth (Fig. 19(b)). Globally, if we compute the relative increase during each time interval

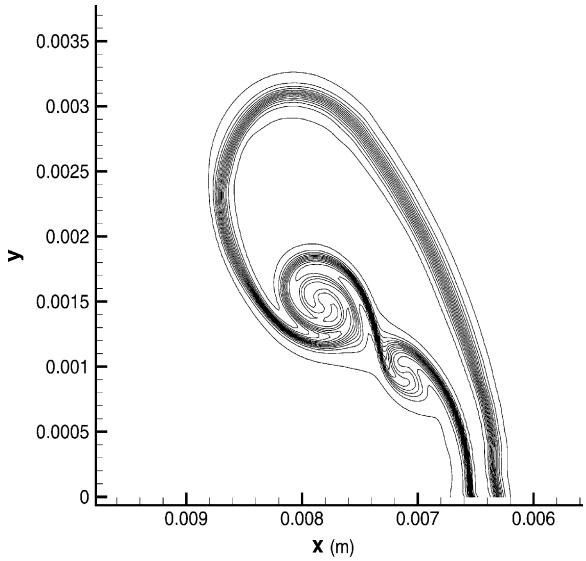

Fig. 20. Hydrogen mass fraction at $t = 1.1 \times 10^{-5}$ s (15 level contours plotted in the range 0.01–0.99).

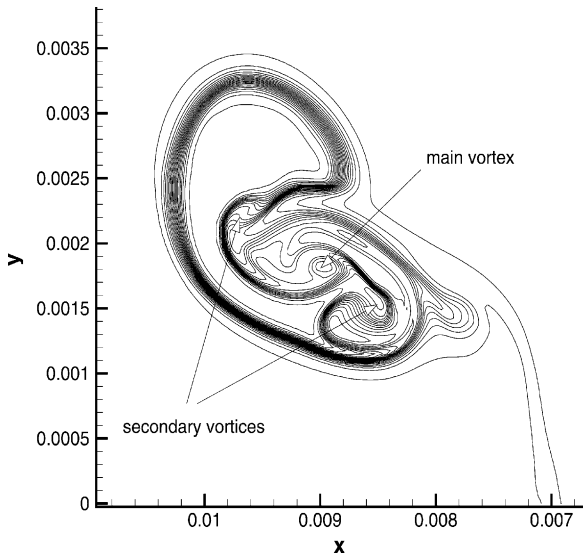

Fig. 21. Hydrogen mass fraction at $t = 1.46 \times 10^{-5}$ s (21 level contours plotted in the range 0.005–0.99).

$$\int_{t_1}^{t_2} \left(\frac{Hr_{\text{wave+flame}} - Hr_{\text{flame}}}{Hr_{\text{flame}}} \right)_{\text{thin flame}} \mathrm{d}t = 2 \times 10^{-3},$$

$$\int_{t_3}^{t_4} \left(\frac{Hr_{\text{wave+flame}} - Hr_{\text{flame}}}{Hr_{\text{flame}}} \right)_{\text{thick flame}} \mathrm{d}t = 1.6 \times 10^{-3},$$

the wave contribution is higher in the emergence period of the flame than when the flame is completely developed.

9.6. Planar shock interacting with a circular hydrogen bubble

At $t = 6 \times 10^{-6}$ s, a circular bubble of hydrogen centered at $(x_c, y_c) = (12\text{ mm}, 0)$ and with radius $r = 2.3$ mm, moving downstream, interacts with a steady Mach 2 planar shock located at $x = 7$ mm. At this time, we are still in the initiation phase of the chemical reactions. The size of the domain is $0 \leqslant x \leqslant 25$ mm and $0 \leqslant y \leqslant 5$ mm and the mesh size is $\Delta x = \Delta y = 25$ μm. A reflection boundary condition is applied at $y = 0$ and Neumann conditions at $y = 5$ mm. NSCBC conditions at $x = 0$ and $x = 25$ mm. Time step δt is driven by the chemical reactions and the production criteria of species Y_{HO_2} and $Y_{H_2O_2}$ (conditions (26) and (27)). During the computation, $10^{-11}\text{ s} \leqslant \delta t \leqslant 5 \times 10^{-10}$ s. The hydrogen and air temperature in the undisturbed region ahead of the shock is set to 1000 K with a pressure of 1 atm. For this simulation, the Reynolds number linked with the main vortex size is $Re_{\text{vortex}} \approx 2800$, the Damköhler number $0.1 \leqslant Da \leqslant 10{,}000$ and the Kolmogorov scale $\eta_k \approx 2.5\ \mu\text{m} = \frac{\Delta x}{10}$.

With this simulation the robustness of this method can be seen as, during the shock bubble interaction, the ratio between the density in the bubble and the density in the air behind the shock goes over 50 on few grid cells. All the computations use uniform Cartesian grid spacing as was done by Don and Quillen [13] and Sjögreen and Yee [14]. The study of the flame structures with complex kinetics, multispecies transport and thermodynamics in great detail requires very small grid mesh. Therefore, the dimensions of our computational domain are smaller than those used in [13,14]. But qualitative comparisons are possible if the number of grid points describing the deformation of the bubble is about the same. A space coordinates change is done because in [13,14], the shock travels and the bubble is unmoved.

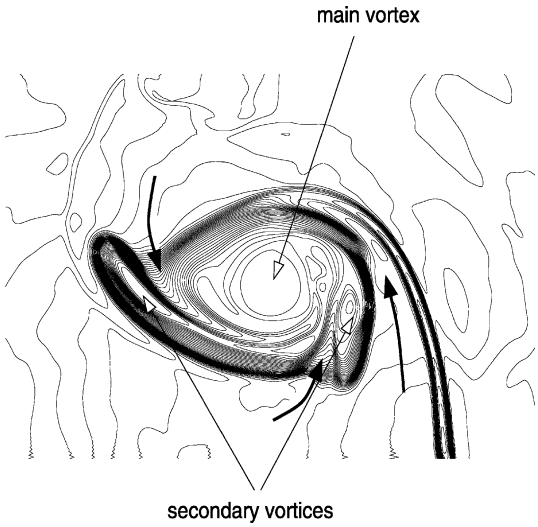

Fig. 22. Density contours at $t = 2.3 \times 10^{-5}$ s, (40 level contours in the range 0.05–1.2 kg/m^3).

In Figs. 20–22, we show the numerical solutions obtained with our method. From a similar grid mesh, these figures may be compared with results obtained in [13] (Fig. 8 bottom, Fig. 9 bottom) for Fig. 20 and in [13] (Fig. 10 bottom, Fig. 11 bottom and Fig. 12 middle) and [14] (Figs. 11(b), 12(b), 13(b) and 14(b)) for Fig. 21. In Fig. 20, as in [13], a jet of air begins penetrating the bubble and is wound round the vortex which sets up at this location. Just below this vortex, we have a second weaker vortex that rolls up the interface. In [13], and particularly with the pseudospectral method, a deformation of the interface in this region may be seen but the presence of this vortex is not as visible as in our simulation, may be because in our simulation

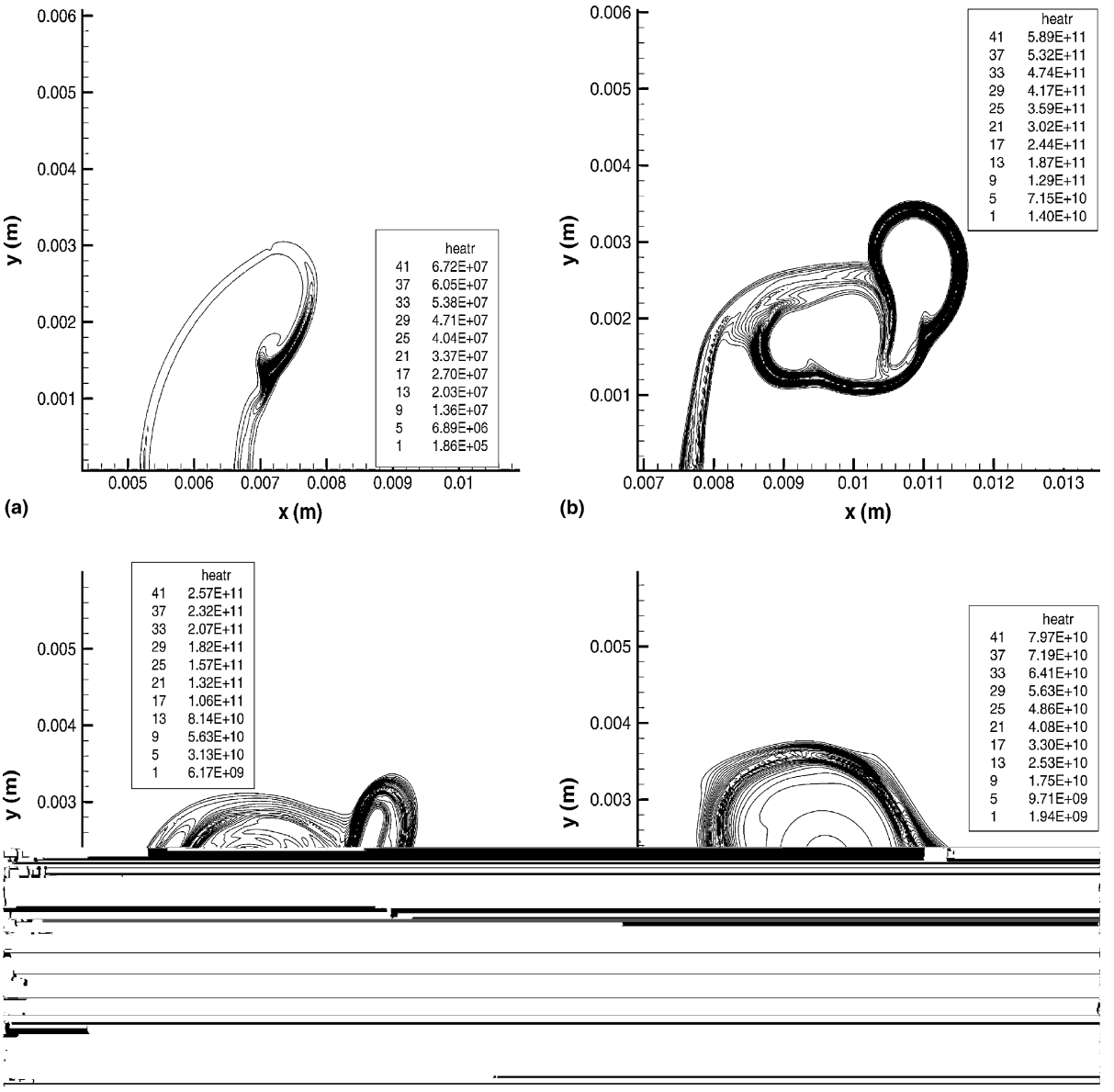

Fig. 23. Heat release rate at different times: (a) $t = 9.2 \times 10^{-6}$ s, (b) $t = 1.66 \times 10^{-5}$ s, (c) $t = 1.98 \times 10^{-5}$ s, (d) $t = 3.42 \times 10^{-5}$ s.

the shock is spread over one or two cells only. This stiffness sets up very strong pressure gradients and consequently, more intense peaks of vorticity than in [13,14] where the shock seems thicker. Fig. 21 shows the air jet that is now in the back side of the bubble. The "mushroom" shape roll-up of the air can be seen clearly and our result is very similar with the results obtained by the pseudospectral approach used in [13]. TVD66-RK4, WENO5-RK4 and ENO3-RK3 are too diffusive and the mushroom shape does not appear. Only ACM66-RK4 [14] captures this phenomenon due to the presence of two vortices (a main vortex with a very strong intensity and a secondary vortex less intense). The finger located in the lower zone of the structure contains a heavy mixture that penetrates in the lighter gas because of the presence of a secondary vortex in this region. As in the pseudospectral approach, our method restores well this feature.

At last, the density is presented in Fig. 22 and may be compared with the contour plots of density drawn by Don and Quillen at $t = 120$ μs (Figs. 6 and 7 in [13]). At this time, the shape of the interface is still very similar with that presented by Don and Quillen. Particularly, our simulation captures the jets of heavy flow into the bubble (represented by arrows) as the pseudospectral does.

In conclusion, our scheme describes the phenomena as well as the pseudospectral method and without having recourse to post-processing. If we study the results presented in [14] with a similar grid mesh, we see that only ACM66-RK4 is able to reproduce the same flow pattern.

With Fig. 23, we come back to the normal coordinates system. Fig. 23 shows the heat release rate at four instants. At $t = 9.2 \times 10^{-6}$ s, we see that the reactions start in the region where the vorticity is highest. At $t = 1.66 \times 10^{-5}$ s, the reactions appear along the interface and in the finger which penetrates in the bubble. The maximum value of the heat release rate is reached around this time. At $t = 1.98 \times 10^{-5}$ s, the flame has a complex shape due to the action of several vortices and at the last time, $t = 3.42 \times 10^{-5}$ s, the main vortex has absorbed the other vortices. The bubble moves as a solid body and the flame is located around the vortex.

Fig. 24 presents the time variation of Hr when the bubble moves in an uniform flow and when it crosses the shock. The presence of the shock involves a much shorter induction time, a much higher maximum value of Hr and globally the heat release is more important than when the flame is in an uniform flow.

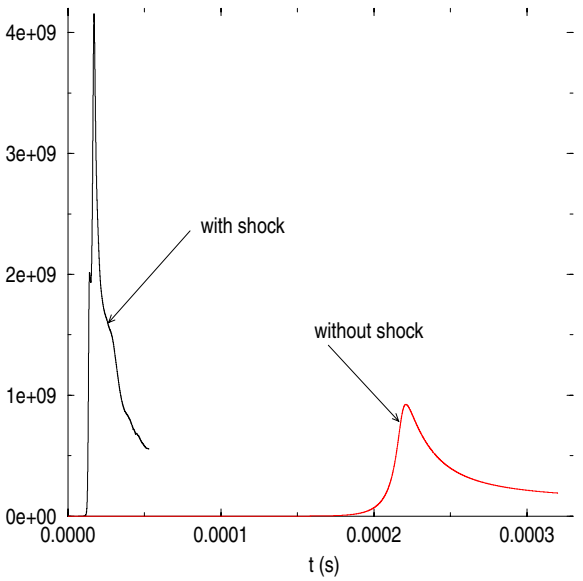

Fig. 24. Hr with and without shock interaction.

Production rates ω_i° are displayed on Fig. 25. If we compared these variations with their variations when the flame is unperturbed, we remark great differences. A strong increase may be observed at $t = 1.2 \times 10^{-5}$ s due to the rapid set up of reactions in the left braid of the structure where the thickness of hydrogen bubble is very thin. After, the flame propagates along all the interface (Fig. 23(b)). During this phase, the reactions are less intense in the braid and the ω_i° decrease during a short time and enhance again when the flame has completely wrapped the bubble at $t = 1.66 \times 10^{-5}$ s (Fig. 23(b)). Then, the production rates decrease but a plateau appears after $t = 1.98 \times 10^{-5}$ s because some reactions are reactivated thanks to vortex actions. The increase of the mixing due to the vortices (Fig. 23(c)) is visible on the production rates of O and OH which

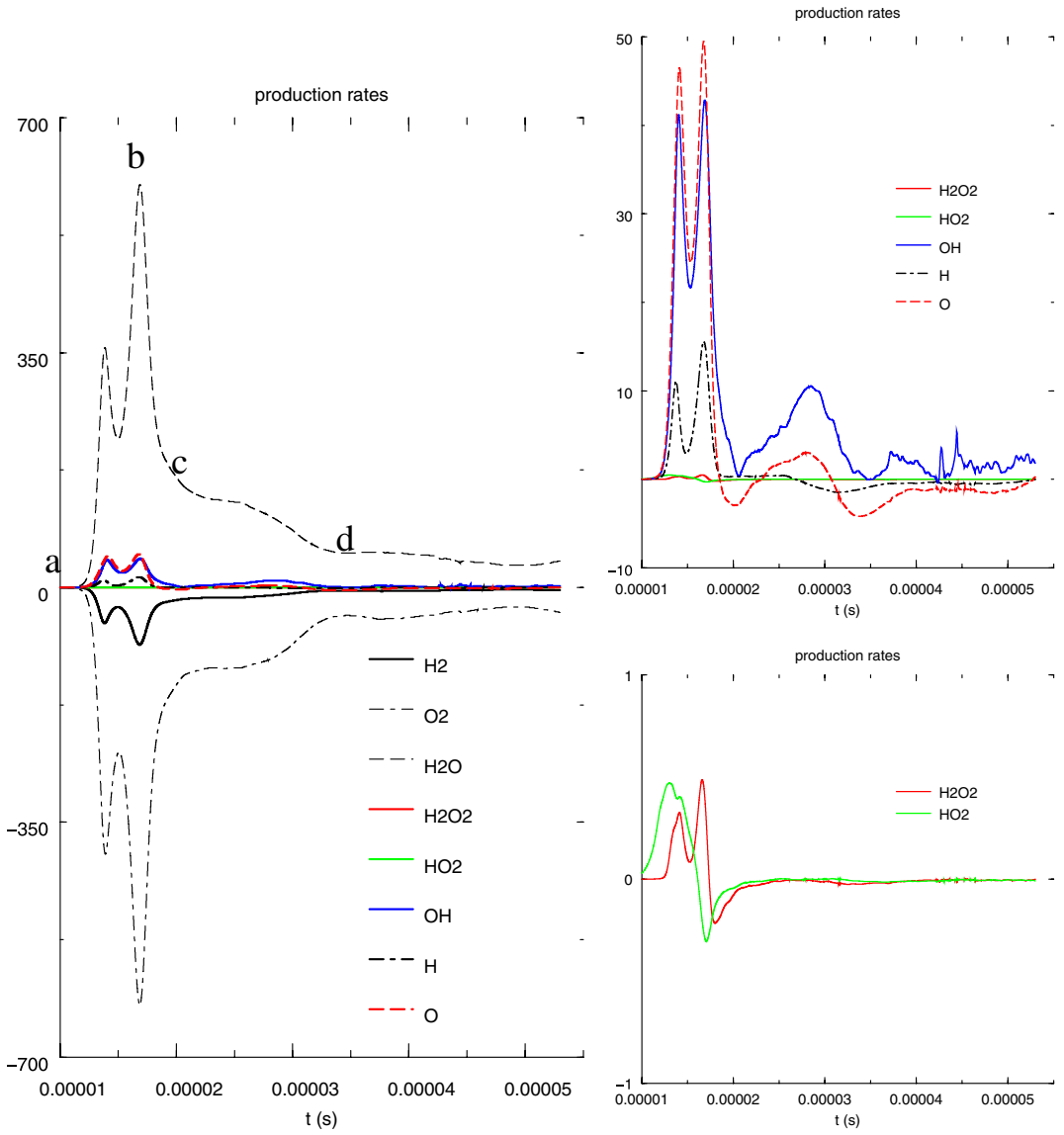

Fig. 25. Time variation of production rates of species.

growth between 2×10^{-6} s and 3×10^{-6} s. After this time, the flame rotates around the vortex (Fig. 23(d)) and the production rate behavior becomes more steady.

10. Computational cost

The computations presented here have been performed on a NEC SX-5. The code has been vectorized and reaches 2.8 Gflops. For one processor, the CPU seconds per time step and per grid mesh is about 3×10^{-6} s to solve 14 equations (3D computations) with all the transport coefficients. In cycle (24), operators $£_H$ $£_P$, and $£_S$ consume, respectively, about 35%, 45% and 20% of the computational time. The most consuming subroutine is the computation of the diffusion velocities (30%). Each processor may realize a computation with a 2×10^6 grid mesh size.

11. Conclusion

In [2], we proposed an approach based on adaptive limiters associated with AUSM$^+$ splitting when the velocity and pressure fields present strong fluctuations. We completed this approach with a double flux method which preserves the pressure and the velocity across the contact discontinuities [3] for the reactive flows. In this paper, we have determined the values of the parameters κ and ω which allows to minimize the lower error terms of the scheme when the velocity and pressure fields are nearly constant.

We have applied this approach with a one step scheme on 1D, 2D and 3D unsteady reactive flows. When it was possible, the results have been compared with those of high-order methods. These comparisons show that our approach is stable (for $C_{cfl} \leqslant 0.7$), sufficiently accurate and is definitely less expensive compared with others methods. The domain of research is enlarged since we may simulate detailed reactive phenomena where high speed flows keep close to low speed flows.

A paper describing in detail the shock–diffusion flame interaction and the ensuing interaction between vortices and diffusion flame is in preparation. Two different cases will be studied. First, when the shock hits the bubble before the reactive process start (as in the case presented here) and secondly, when the shock goes through the bubble during the reactive process. The effects due to the thermodiffusion, the barodiffusion and the bulk viscosity will be studied.

References

[1] B. Van Leer, Towards the ultimate conservative difference scheme. V. A second order sequel to Godunov's method, J. Comput. Phys. 32 (1979) 101.
[2] G. Billet, O. Louédin, Adaptive limiters for improving the accuracy of the MUSCL approach for unsteady flows, J. Comput. Phys. 170 (2001) 161–183.
[3] G. Billet, R. Abgrall, An adaptive shock-capturing algorithm for solving unsteady reactive flows, Comput. Fluids 32 (2003) 1473–1495.
[4] M.S. Liou, A sequel to AUSM: AUSM$^+$, J. Comput. Phys. 129 (1996) 364.
[5] C. Hirsch, Numerical Computation of Internal and External Flows, Wiley, 1992.
[6] E. Godlewski, P.A. Raviart, Hyperbolic Systems of Conservation Laws, Ellipses, 1990.
[7] P.K. Sweby, High resolution scheme using flux limiters for Hyperbolic conservation laws, SIAM J. Numer. Anal 21 (1984) 995–1011.
[8] E.S. Oran, P.B. Boris, Numerical Simulation of Reactive Flow, Elsevier, Amsterdam, 1987.
[9] D. Thévenin, F. Behrendt, U. Mass, B. Przywara, J. Warnatz, Development of a portable parallel direct simulation code to investigate reactive flows, Comput. Fluids 25 (5) (1996) 485–496.

[10] J.A. Miller, R.E. Mitchell, M.D. Smooke, R.J. Kee, Toward a comprehensive chemical kinetic mechanism for the oxidation of acetylene: comparison of model predictions with results from flame and shock tube experiments, in: Nineteenth Symposium on Combustion, Combustion Institute, 1982, pp. 181–196.
[11] P. Laval, New splitting-up schemes for solving hyperbolic and parabolic non-linear problems: applications to Euler and Navier–Stokes equations, Rech. Aérosp. 1983-4 (1983).
[12] G. Billet, Study of transient turbulent non-reactive and reactive flow at large Reynolds number with a temporal filtered LES, Technical note ONERA 1996-3, 1996.
[13] W.S. Don, C.B. Quillen, Numerical simulation of shock-cylinder interactions, I. Resolution, J. Comput. Phys. 122 (1995) 244–265.
[14] B. Sjögreen, H.C. Yee, Grid convergence of high order methods for multiscale complex unsteady viscous compressible flows, J. Comput. Phys. 185 (2003) 1–26.
[15] M. Baum, T. Poinsot, D. Thévenin, Accurate boundary conditions for multicomponent reactive flows, J. Comput. Phys. 116 (1994) 247–261.
[16] A. Laverdant, D. Thévenin, Interaction of a gaussian acoustic wave with a turbulent premixed flame, Combust. Flame 134 (2003) 11–19.